Quantifying the cool ISM in radio AGNs: evidence for late-time re-triggering by galaxy mergers and interactions

E. Bernhard[1]⋆, C. N. Tadhunter[1], J. C. S. Pierce[1,2], D. Dicken[3], J. R. Mullaney[1], R. Morganti[4], C. Ramos Almeida[5,6], and E. Daddi[7]

[1] *Department of Physics & Astronomy, University of Sheffield, Sheffield S3 7RH, UK*
[2] *Centre for Astrophysics Research, University of Hertfordshire, College Lane, Hatfield AL10 9AB, UK*
[3] *Institut d'Astrophysique Spatiale, CNRS, Univ. Paris-Sud, Université Paris Saclay, Bâtiment 121, 91405 Orsay Cedex, France*
[4] *ASTRON, the Netherlands Institute for Radio Astronomy, Oude Hoogeveensedijk 4,7991 PD Dwingeloo, The Netherlands*
[5] *Instituto de Astrofísica de Canarias, Calle vía Láctea, s/n, 38205 La Laguna, Tenerife, Spain*
[6] *Departamento de Astrofísica, Universidad de La Laguna, 38206, La Laguna, Tenerife, Spain*
[7] *CEA, IRFU, DAp, AIM, Université Paris-Saclay, Université Paris Diderot, Sorbonne Paris Cité, CNRS, F-91191 Gif-sur-Yvette, France*

ABSTRACT

We use deep *Herschel* observations of the complete 2Jy sample of powerful radio AGNs in the local universe ($0.05 < z < 0.7$) to probe their cool interstellar medium (ISM) contents and star-forming properties, comparing them against other samples of nearby luminous AGNs and quiescent galaxies. This allows us to investigate triggering and feedback mechanisms. We find that the dust masses of the strong-line radio galaxies (SLRGs) in our sample are similar to those of radio-quiet quasars, and that their median dust mass ($M_{\rm dust} = 2 \times 10^7\ M_\odot$) is enhanced by a factor ∼200 compared to that of non-AGN ellipticals, but lower by a factor ∼16 relative to that of local ultra-luminous infrared galaxies (UILRGs). Along with compelling evidence for merger signatures in optical images, the SLRGs in our sample also show relatively high star-formation efficiencies, despite the fact that many of them fall below the main sequence for star forming galaxies. Together, these results suggest that most of our SLRGs have been re-triggered by late-time mergers that are relatively minor in terms of their gas contents. In comparison with the SLRGs, the radio AGNs with weak optical emission lines (WLRGs) and edge-darkened radio jets (FRIs) have both lower cool ISM masses and star-formation rates (by a factor of >30), consistent with being fuelled by a different mechanism (e.g. the direct accretion of hot gas).

Key words: galaxies: active, galaxies: ISM, galaxies: quasars: general, galaxies: starburst, galaxies: interactions

1 INTRODUCTION

Despite the importance of supermassive black hole growth in regulating galaxy evolution via active galactic nucleus (AGN) feedback (see Harrison 2017 for a review), AGN triggering mechanisms remain a highly debated subject. In this context, powerful radio AGNs are particularly important. On the one hand, they are almost invariably hosted by elliptical galaxies, allowing for relatively "clean" searches to be made for the morphological signatures of the triggering events (e.g. tidal tails and shells); any cool gas detected in such galaxies is also more likely to have an external origin than in late-type galaxies. On the other hand, radio AGNs launch powerful relativistic jets that are capable of heating

the large-scale inter-stellar/galactic medium (ISM/IGM) – one of the most important forms of AGN feedback (e.g. Best et al. 2006; McNamara & Nulsen 2007).

Deep observational campaigns undertaken at optical wavelengths have reported that signatures of galaxy interactions are common amongst samples of local powerful radio AGNs (e.g. Heckman et al. 1986; Smith & Heckman 1989; Ramos Almeida et al. 2011; Ramos Almeida et al. 2012; Pierce et al. 2021). However, these optical features do not correspond to a single merger phase (i.e. pre-or-post merger) or type (i.e. minor/major), thereby questioning the link between radio AGN activity and the peaks of major gas-rich galaxy mergers[1], as represented by ultra-luminous infrared

---

⋆ E-mail: e.p.bernhard@sheffield.ac.uk

[1] Hereafter, we refer to the peaks of major gas-rich galaxy

galaxies (ULIRGs; Sanders et al. 1988; Sanders & Mirabel 1996). In addition, a higher fraction of merger signatures were found amongst powerful radio AGNs associated with strong optical emission lines (i.e. strong-line radio galaxies and high-excitation radio galaxies; SLRGs and HERGs), typical of those observed in quasars (QSOs), when compared to radio AGNs lacking such optical features (i.e. weak-line radio galaxies and low-excitation radio galaxies; WLRGs and LERGs; e.g. Malin & Carter 1983; Ramos Almeida et al. 2011; Pierce et al. 2021)[2]. This potentially implies different dominant triggering mechanisms for SLRGs and WLRGs, linking the most major gas-rich mergers with the former population of radio AGNs. However, it is difficult to quantify the nature of the merger (i.e. major/minor and gas-rich/poor) from optical images alone.

With the advancement of mid-to-far-infrared astronomy via observatories such as the Wide-field Infrared Survey Explorer (*WISE*; Wright et al. 2010), *Spitzer* (Werner et al. 2004), and *Herschel*[3] (Pilbratt et al. 2010), it is now possible to trace the dust content of galaxies, a proxy for the overall cool interstellar medium (ISM) contents (e.g. Draine & Li 2007; Parkin et al. 2012; Rémy-Ruyer et al. 2014). This provides information on the nature of the merger by comparing the cool ISM content of powerful radio-loud AGNs with that expected from major gas-rich galaxy mergers, therefore complementing results from optical images. In a preliminary study, Tadhunter et al. (2014) found that the median dust mass of nearby SLRGs is lower than that of ULIRGs, therefore emphasising the importance of more minor mergers in triggering such objects.

The star-forming properties of host galaxies also provide key information on AGN triggering mechanisms. Most star-forming galaxies follow a redshift-dependent relationship between star formation rate (SFR) and stellar mass (e.g. Daddi et al. 2007; Elbaz et al. 2007; Noeske et al. 2007; Rodighiero et al. 2014; Sargent et al. 2014; Schreiber et al. 2015), known as the main sequence (MS) of galaxies. A small fraction ($\sim$3 per cent), mainly triggered by major gas-rich galaxy mergers, and referred to as star-bursting systems, show SFRs at least a factor of 4 above the MS (e.g. Sargent et al. 2014; Schreiber et al. 2015). Therefore, comparing the star-forming properties of the hosts of powerful radio-loud AGNs to the MS of galaxies can provide further information on their triggering mechanisms.

Here, using deep *Herschel* far-infrared (FIR) data for a unique sample of nearby (i.e. $z < 0.7$) powerful radio AGNs (the 2Jy sample; see § 2.1.1 for details), combined with the abundance of complementary multi-wavelength data available for this sample, we investigate the triggering mechanisms of powerful radio AGNs, split in terms of SLRGs and WLRGs. To do this, we measure their cool ISM properties, SFRs, and SFR efficiencies, and compare them against those of samples of radio-quiet QSOs, non-AGN classical elliptical galaxies, and ULIRGs. We further place the SFRs in the context of the MS of star-forming galaxies to provide a more complete picture of the triggering and feedback mechanisms of powerful radio AGNs.

This paper is organised as follows. We present in § 2 our samples of powerful radio AGNs and comparison samples. We show in § 3, § 4, and § 5 how we calculated dust masses, SFRs and stellar masses, respectively. Our results on the dust masses and the SFRs are presented in § 6, and their implications in § 7. Finally, we present the main concluding remarks in § 8. Throughout, we adopted a WMAP–9 year cosmology ($H_0 = 69.3\,\mathrm{km\,s^{-1}\,Mpc^{-1}}$, $\Omega_m = 0.29$, $\Omega_\Lambda = 0.71$; Hinshaw et al. 2013)[4] and a Chabrier (2003) initial mass function when calculating galaxy properties.

2   DATA AND SAMPLES

In this section we present our samples of powerful radio AGNs and the comparison samples for which we derive dust masses (M_{dust}) and SFRs. The main method adopted to calculate M_{dust} relies on the 100 and 160 μm fluxes and their ratio (see § 3), since these are now available for large samples of nearby objects. Therefore, our primary selection is based on the availability of *Herschel*-PACS (Poglitsch et al. 2010) fluxes at 100 or 160 μm. For objects with additional *Herschel*-SPIRE data (i.e. at 250, 350, and 500 μm; Griffin et al. 2010), we constructed infrared (IR) spectral energy distributions (SEDs) to fit detailed dust emission models (see § 3.1). For these we also included the *Herschel* fluxes at 70 μm when available, and we required an additional mid-IR (MIR) data point to account for any potential warmer dust contributions (see § 3.1.1). Overall, sources selected for detailed SED fits fulfilled all of the following criteria as a minimum requirement,

- detected with *Spitzer* at 24 μm *or WISE* at 22 μm;
- detected with *Herschel*–PACS at 100 μm or 160 μm;
- detected with *Herschel*–SPIRE at 250 μm *and* 350 μm.

These SED fits provide more precise estimates of M_{dust} values, which, once compared with those estimated from the 100/160 μm flux ratio method (see § 3.2), allows us to test the latter.

To calculate SFRs, we used a multi-component SED fitting code which accounts for AGN contribution when necessary (see § 4). Therefore, for these SFR estimates, we also considered archival *WISE*, *Spitzer*–MIPS (Fazio et al. 2004) and *Spitzer*–IRAC (Rieke et al. 2004) data from the NASA/IPAC IR Science Archive (IRSA) at wavelengths of 8–24 μm. Only sources with robust quality flags were used[5],

---

merger to differentiate from galaxy interactions at pre/post galaxy merger and more minor mergers.

[2] In this work, we use the SLRG/WLRG classification, where SLRGs have EW$_{\mathrm{[OIII]}} > 10$ Å.

[3] *Herschel* is an ESA space observatory with science instruments provided by European-led Principal Investigator consortia and with important participation from NASA.

[4] We stress that these are the default values for the WMAP–9 year cosmology of the PYTHON package ASTROPY (Astropy Collaboration et al. 2018).

[5] For the *WISE* data, where extended sources were flagged, we used the photometry calculated within the extended 2MASS aperture when available. Otherwise, when the extended flag was set to 1, we checked the reduced chi-squared value (χ^2_ν) of the profile fit, and only used the flux if $\chi^2_\nu < 3$. For the *Spitzer*–MIPS and –IRAC data, only point sources were used, and the fluxes of extended sources were discarded.

Table 1. Table summarising our various populations and samples of AGNs and galaxies, as described in § 2. Here, "RL", "RQ" and "E." correspond to radio-loud, radio-quiet, and ellipticals. We also indicate where the *Herschel* IR fluxes were taken from (i.e. "C14": Ciesla et al. 2014, "W16": Westhues et al. 2016, "S18": Shangguan et al. 2018, "S19": Shangguan & Ho 2019, "D21": Dicken et al., in prep., and/or HPDPs), as well as some sample statistics: the total number of sources retained in each sample ($N_{\rm tot}$), of which the number selected for SED fits ($N_{\rm fit}$; see § 2), and the fractions detected at both 100 and 160 μm, as well as the fractions detected at one band only, respectively. We note that the large fractions of detected sources in the Atlas$^{\rm 3D}$ sample arise due to selection effects, and do not reflect the true fractions of IR detected elliptical galaxies in this sample. The K17* corresponds to the extra sources with dust masses reported in Kokusho et al. (2019) and based on AKARI fluxes measured in Kokusho et al. (2017) for the Atlas$^{\rm 3D}$ sample, and that we have included in our analysis (see § 2.4.1).

Types	Samp.	Ref. IR	$N_{\rm tot}$	$N_{\rm fit}$	IR det. 2 bands	IR det. 1 band
RL AGNs	2Jy	D21	46	8	89%	11%
	3CR	W16	45	4	47%	29%
RQ QSOs	PGQs	S18	70	9	86%	10%
	Type-II	S19	86	12	82%	13%
ULIRGs	HERUS	C18 HPDPs	41	14	51%	49%
E. Gal.	Atlas$^{\rm 3D}$	HPDPs	6	4	67%	33%
		K17*	32	–	–	–
	HRS	C14 HPDPs	8	0	0%	0%

as described in the explanatory supplements of each instrument available on the IRSA website[6].

We provide in Table 1 a full listing of our various populations of AGNs and galaxies, as presented in the following subsections. In addition, detailed Tables listing the general properties of each of the objects in these samples are accessible in the online material.

2.1 Powerful radio-loud AGNs

Our main samples consist of nearby radio-loud AGNs. As they are almost invariably hosted in elliptical galaxies (e.g. Tadhunter 2016; Pierce et al. 2021), they offer a clean way to search for signs of interactions and investigate triggering and feedback mechanisms (see § 1).

2.1.1 The 2Jy sample

Our primary radio AGN sample comprises 46 nearby ($0.05 < z < 0.7$) southern ($\delta < 10°$) powerful radio galaxies with steep radio spectra ($F_\nu \propto \nu^{-\alpha}$; $\alpha > 0.5$) from the 2Jy sample of Wall & Peacock (1985), complete at

[6] Available at `https://wise2.ipac.caltech.edu/docs/release/allwise/expsup/index.html` for *WISE*, and at `https://irsa.ipac.caltech.edu/data/SPITZER/Enhanced/SEIP/docs/seip_explanatory_supplement_v3.pdf` for *Spitzer*.

$S_{\rm 2.7GHz} > 2$ Jy (Dicken et al. 2009). This sample is unique in the depth and completeness of its multi-wavelength data, in particular at mid-to-far-IR wavelengths. Deep *Herschel* photometry is now available for the 2Jy sample, following observations performed between October 2012 and March 2013 as part of program DDT_mustdo_4. While preliminary results for the *Herschel* data were presented in Tadhunter et al. (2014), the detailed observation strategy, data reduction, and the most recent fluxes will be reported in Dicken et al. (subm.). Crucially, in the latter, efforts were made to calculate IR fluxes free of non-thermal contamination, which can be a particular issue for radio-loud AGNs in the FIR.

All of the 46 sources were detected at 100 μm, and 41 (89 per cent) were also detected at 160 μm. However, we treated the FIR fluxes of 14 sources (30 per cent) as upper limits, since they showed potential non-thermal contamination that could not be corrected for (Dicken et al., subm.; see also Tables in the online material). Out of the full sample of 46 sources, eight were selected for detailed SED fits based on the criteria outlined at the beginning of § 2.

For this sample, we also have radio morphologies separated between FRIs and FRIIs (following Fanaroff & Riley 1974) based on the radio observations of Morganti et al. (1993, 1999), [OIII]$_{\lambda_{5007\text{Å}}}$ luminosities ($L_{\rm [OIII]}$) and optical classes (i.e. SLRG/WLRGs) based on the optical spectroscopic data of Tadhunter et al. (1993, 1998). Preliminary results on the dust masses of the SLRGs in this sample were presented in Tadhunter et al. (2014).

2.1.2 The 3CR sample

We further considered the Revised Third Cambridge Catalogue of Radio Sources (Bennett 1962a,b; Spinrad et al. 1985, 3CR), which is a flux-limited sample of bright ($S_{\rm 178Mhz} > 9$ Jy) northern ($\delta > -5°$) radio AGNs. The 3CR sample is similar to the 2Jy sample in terms of radio power, but selected at lower frequencies. Although less complete in terms of detections at FIR wavelengths (see below), it provides an important check on the results for the 2Jy sample, using a sample of powerful radio AGNs selected at a different frequency. A representative sub-sample of 48 3CR sources at $z < 0.5$ have been observed with *Herschel*, and the fluxes and upper limits are reported in Table 4 of Westhues et al. (2016).

We removed 3C 459.0 as it is the same object as PKS 2314+03 from the 2Jy sample (see § 2.1.1). Out of the 47 unique remaining 3CR sources, 29 (62 per cent) were detected at 100 μm, of which 22 (47 per cent) were also detected at 160 μm. The *Herschel* observations of the 3CR sample are shallower than those of the 2Jy, hence the lower detection rates. Including upper limits, we found 41 sources (87 per cent) with fluxes or upper limits at 100 or 160 μm. For an extra four sources without *Herschel*–PACS fluxes in Westhues et al. (2016), we found archival Infrared Astronomical Satellite (*IRAS*) fluxes at 100 μm from NED, one of which is an upper limit. Therefore, out of our sample of 47 unique 3CR sources, 45 were retained.

The possibility of non-thermal contamination was addressed by collecting archival measurements at $\lambda > 500\ \mu$m (e.g. from the Very Large Array, the Very Long Baseline Array, and the IRAM 30-meter telescope) from the NASA/IPAC Extragalactic Database (NED), separating the

core and the extended emission (lobe/hotspot), when possible. A power-law with free spectral index was fit to the extended component, and extrapolated down to 100 μm. For the core, we took the level of non-thermal flux found at longer wavelengths and extrapolated this down to 100 μm, assuming a flat spectrum. If the extrapolated fluxes (i.e. from the extended and/or core emission) at any of the *Herschel* wavelengths were above 10 per cent of the observed fluxes, the source was considered as potentially contaminated by non-thermal emission. However, for sources showing apparent non-thermal contamination from the extended radio lobes only, we compared the radio maps against the size of the *Herschel* beams. If the *Herschel* beams were smaller than the bulk of extended non-thermal emission, the fluxes were considered free of non-thermal contamination.

The FIR fluxes contaminated by non-thermal emission, either from the core and/or for which the *Herschel* beams potentially contained the extended non-thermal emission, were treated as upper limits. Amongst the 45 radio AGNs in the 3CR sample, the FIR fluxes for six objects (13 per cent of the full 3CR sample and 24 per cent of the detected sources) were treated as upper limits to account for the potential non-thermal contamination. Overall, four 3CR sources were selected for detailed SED fits based on the criteria outlined at the beginning of § 2, one of which includes the *IRAS* flux at 100 μm.

The 3CR objects at $z \lesssim 0.3$ were originally classified as LERGs or HERGs by Buttiglione et al. (2009, 2010, 2011), but then re-classified as SLRGs or WLRGs by Tadhunter (2016). Although LERG/HERG and WLRG/SLRG classification schemes show considerable overlap, they are not exactly the same (see discussion in Tadhunter 2016). For this work, we use the WLRG/SLRG classifications of the 3CR sources, for which we also have radio classes (FRI/FRII) and [OIII] luminosities. We also found archival[7] radio classes and $L_{[OIII]}$ values for all of the remaining 3CR sources in Westhues et al. (2016) with $z \gtrsim 0.3$.

2.2   Radio-quiet QSOs

To test whether the cool ISM and star-forming properties of radio-loud and radio-quiet AGNs are different, perhaps related to distinct triggering mechanisms, we also constructed comparison samples of optically unobscured (Type-I) and obscured (Type-II) radio-quiet QSOs.

2.2.1   The Type-I PG QSO sample

For our comparison sample of Type-I QSOs, we used the 87 nearby (z < 0.5) UV/optically selected QSOs from the Palomar-Green (PG) survey of Schmidt & Green (1983) with B < 16.17 (e.g. Goldschmidt et al. 1992). The PG QSO (PGQ) sample is representative of bright, nearby Type-I (unobscured) QSOs and benefits from a plethora of multi-wavelength data.

After removing the 16 radio-loud PGQs (as classified according to the criteria of Boroson & Green 1992), we were left with 71 objects. We adopted the *Herschel* fluxes listed in Shangguan et al. (2018; and references therein), and found 68 sources (96 per cent) detected at 100 μm, of which 60 (84 per cent) were also detected at 160 μm. For all of the remaining sources, but one not observed with *Herschel–*PACS, we used the upper limits as reported in Shangguan et al. (2018). Therefore, our final PGQ sample contained 70 sources, of which nine were selected for detailed SED fits based on the criteria outlined at the beginning of § 2. For the full PGQ sample we have [OIII] luminosities, and estimates of the dust and stellar masses (Shangguan et al. 2018).

2.2.2   The Type-II QSO sample

For our comparison sample of Type-II QSOs, we used that defined in Shangguan & Ho (2019), and originally taken from the Sloan Digital Sky Survey (SDSS; Reyes et al. 2008). It contains 86 randomly selected sources that match the PGQ sample of Shangguan et al. (2018), in redshift (at z < 0.5) and [OIII] luminosity ($10^{8.0}$ < $L_{[OIII]}/L_{\odot}$ < $10^{9.8}$; see Shangguan & Ho 2019, for details on the selection technique). We used the *Herschel* fluxes reported in Shangguan & Ho (2019), and found 82 sources (95 per cent) detected at 100 μm, of which 71 (82 per cent) were also detected at 160 μm. For the remaining sources we used the upper limits on the *Herschel–*PACS fluxes reported in Shangguan & Ho (2019). This sample is representative of bright, nearby Type-II QSOs.

According to Shangguan & Ho (2019), none of these sources were found to show significant non-thermal contamination at IR wavelengths. As for the PGQs, we also have [OIII] luminosities, and dust and stellar mass estimates for the Type-II QSOs (see Shangguan & Ho 2019, for details). Out of the 86 objects, 12 were selected for detailed SED fits based on the criteria outlined at the beginning of § 2.

2.3   Ultra Luminous IR Galaxies

We defined a comparison sample of ULIRGs which traces the cool ISM content of galaxies at the peaks of major gas-rich mergers. This allows us to assess the importance of major gas-rich mergers for triggering the powerful radio AGNs in our samples, by comparing their cool ISM properties against those of ULIRGs[8].

We used the *Herschel* ULIRG survey (HERUS, PI D. Farrah, programme ID OT1_dfarrah_1), which is an unbiased sample of 43 nearby (z < 0.3) ULIRGs with *IRAS* 60 μm fluxes > 1.8 Jy, and originally identified in the *IRAS* Point Source Catalogue Redshift (PSC-z) survey of Saunders et al. (2000). The ULIRGs Mrk 1014 and 3C 273.0 were removed from this sample, as they correspond to AGNs found in our PGQ (§ 2.2.1) and 3CR (§ 2.1.2) samples, respectively.

---

[7] Leahy et al. (1986), Leahy & Perley (1991), Gelderman & Whittle (1994), Giovannini et al. (1994), Jackson & Rawlings (1997), Mack et al. (1997), Ludke et al. (1998), Haas et al. (2005), Koss et al. (2017), R.A. Laing (unpublished), and D.A. Clarke and J.O. Burns (unpublished).

[8] We stress that, although the majority of ULIRGs are likely to represent the peaks of major, gas-rich mergers, not all such mergers necessarily lead to the levels of star formation and AGN activity observed in ULIRGs. However, all major, gas-rich mergers would be expected to have substantial (ULIRG-like) reservoirs of cool ISM.

For the *Herschel*–PACS data, we cross-matched the ULIRG sample with archival *Herschel* data from the Highly Processed Data Products (HPDPs), available on the IRSA website, which offer the most complete and uniform database of reduced fluxes for *Herschel*–PACS (Marton et al. 2017) and *Herschel*–SPIRE (Schulz et al. 2017)[9]. We found 19 sources (46 per cent) observed and detected at 100 and 160 μm. For all of the remaining sources (54 per cent), we used the original *IRAS* fluxes at 100 μm (and 60 μm for the SED fits). This sample was also observed by *Herschel*–SPIRE, with all of the 41 sources being detected, and with fluxes reported in the Table 2 of Clements et al. (2018; originally from Pearson et al. 2016). Finally, 14 of the ULIRGs were selected for detailed SED fits based on the criteria outlined at the beginning of § 2.

2.4 Classical elliptical galaxies

As powerful radio AGNs are almost invariably hosted by elliptical galaxies, we defined samples of non-AGN classical elliptical galaxies to compare against.

2.4.1 The Atlas[3D] sample

Our first sample was selected from the Atlas[3D] survey, which is a volume limited (D < 42 Mpc, M_K < −21.5) sample of 260 nearby morphologically-selected early-type galaxies (Cappellari et al. 2011). We only retained the 68 objects that were classed as elliptical (i.e. T-Type $\lesssim$ -3.5 in Cappellari et al. 2011, excluding S0 galaxies) to match the morphology of the hosts of powerful radio AGNs.

We cross-matched this sample against archival *Herschel* data from the HPDPs (see § 2.3 for the HPDPs), and, out of the 25 objects observed with *Herschel*, six (30 per cent) had reliable detected fluxes at 100 μm, of which four (20 per cent) were also detected at 160 μm. In total, seven galaxies were at least detected at 100 or 160 μm. We removed NGC 4374 as it showed an inflection at *Herschel*-SPIRE wavelengths, which is a potential sign of non-thermal AGN contamination.

Therefore, our full sample of elliptical galaxies from the Atlas[3D] survey contained six objects, of which four were selected for detailed SED fits based on the criteria outlined at the beginning of § 2. We note that, as a consequence of using only elliptical galaxies detected at FIR wavelengths, this sample is likely biased toward the nearby non-AGN elliptical galaxies that are brightest at FIR wavelengths.

The Atlas[3D] survey further benefits from IR observations taken with AKARI at 9, 18, 65, 90, and 140 μm (Kokusho et al. 2017). Using the latter, dust masses were calculated in Kokusho et al. (2019). We benefited from the agreement between the dust masses measured with *Herschel* and AKARI (see § 3.2.2) to significantly increase the size of our sample of non-AGN elliptical galaxies. To do this, we included an extra 32 elliptical galaxies (i.e. excluding S0) that were not observed by *Herschel*, but had measured dust masses (11 as upper limits) derived from the AKARI observations and listed in Kokusho et al. (2019).[10] We note that the AKARI data are much less sensitive than the *Herschel* observations. However, they are more complete in their coverage of the Atlas[3D] sample.

2.4.2 The Herschel Reference Survey sample

To further increase the statistics of our sample of classical elliptical galaxies, we used the Herschel Reference Survey (HRS). This is a volume limited sample (i.e. 15 $\lesssim$ D $\lesssim$ 25 Mpc) of 323 galaxies (Boselli et al. 2010), of which 62 are early-types with 2MASS K-band magnitudes K_S ≤ 8.7 mag, after the revised classification of Smith et al. (2012). We only retained the nine objects which are classified as classical ellipticals, and which do not show any signs of AGN activity, as reported in Smith et al. (2012), and references therein.

Using the fluxes taken from Smith et al. (2012), out of these nine sources, three (33 per cent) were detected with *IRAS* at 100 μm, and the rest had flux upper limits, either from *IRAS* (1 source) or from *Herschel* (5 sources). Two sources were also detected at 160 μm with *Herschel*, and five had upper limits. We cross-matched this sample with the *Herschel*-SPIRE fluxes presented in Ciesla et al. (2014), and found that all were constrained by flux upper limits only at longer FIR wavelengths. Therefore, none were selected for detailed SED fits based on the criteria outlined at the beginning of § 2. In addition, we have removed NGC 4649 from the sample as we found large systematic offsets between the *IRAS* flux at 100 μm and the *Herschel* fluxes, suggesting a flux calibration error. We were therefore left with eight sources, mostly constrained by upper limits alone.

3 MEASURING DUST MASSES

In this work, we aim to probe the cool ISM content of powerful radio AGNs by measuring their dust masses, and comparing against those of radio-quiet QSOs, ULIRGs, and non-AGN classical elliptical galaxies (see § 2 for the samples).

The dust masses of the galaxies were calculated using (e.g. Mattsson et al. 2015),

$$M_{\rm dust} = \frac{S_{160}\,d^2}{\kappa_{160}\,B_\nu(160,T)\,(1+z)}\,M_\odot, \qquad (1)$$

where S_{160} is the measured flux at the wavelength that 160 μm is shifted to in the observer's frame, d is the luminosity distance, κ_{160} is the opacity of the dust grains at

---

[9] As found in Bernhard et al. (2021), some nearby sources can be misclassified as point sources in the HPDPs, systematically under-estimating their fluxes. For these, we have corrected the fluxes for missed extended emission, as described in Appendix A of Bernhard et al. (2021).

[10] We note that, originally, there were 39 elliptical galaxies with measured $M_{\rm dust}$ in Kokusho et al. (2019), including the 11 upper limits, that could have been included in our sample since not observed with *Herschel*. However, seven sources with measured dust masses in Kokusho et al. (2019) appeared with fluxes that were not detected (i.e. < 1σ) at any of the AKARI wavelengths in Kokusho et al. (2017). This led to unphysical values for the dust masses of these seven objects. Because the reasons behind this discrepancy are unclear, we have excluded these objects from our sample. We only retained objects that were at least detected in one AKARI band (at > 2σ).

160 μm, and $B_\nu(160, T)$ is the specific intensity of a black-body curve evaluated at 160 μm, and for a given dust temperature, T.[11] $B_\nu(160, T)$ requires the determination of the temperature of the dust. To do this, we employed two different methods. For the sub-sample of objects that were selected for detailed SED fits (based on the criteria outlined in §2), $B_\nu(160, T)$ was measured after performing full IR SED fits, as fully described in §3.1. For the rest of our objects, we developed a method to calculate T mostly based on the 100/160 μm flux ratios, and following that used in Tadhunter et al. (2014), but calibrated using our $M_{\rm dust}$ measured from the detailed SED fits, as fully described in §3.2. We stress that, for consistency, we will use values of $M_{\rm dust}$ measured from the 100/160 μm flux ratios across all of our samples while comparing their cool ISM content, and IR SED fits were only used to test the flux ratio technique.

We also assumed a value for the opacity of the dust grains at 160 μm, κ_{160} (Eq. 1), a parameter which is known to be highly uncertain (see Fig. 1 of Clark et al. 2016 for different values of the dust grain opacities across various studies). The values of κ_{160} that are often quoted in studies of galaxies (e.g. James et al. 2002; Draine 2003; Clark et al. 2016) differ by up to a factor of 3.5. For consistency, we adopted a single value of the dust opacity throughout ($\kappa_{160} = 1.038$ m^2 kg^{-1} from Draine 2003), which is identical to that used in our various comparison studies (see §3.2.2).

3.1 The dust masses from SED fits

3.1.1 Infrared SED fits

To first order, the thermal dust emission of galaxies can be represented by a modified black-body curve with temperature T and beta index β (e.g. Galliano et al. 2018):

$$S_\nu(\nu, T, \beta) = A_{\rm norm} \times \nu^\beta \times B_\nu(\nu, T), \qquad (2)$$

where S_ν is the flux density, $B_\nu(\nu, T)$ is the specific intensity of a black-body curve at temperature T, and $A_{\rm norm}$ is a constant of normalisation. However, the full IR emission of galaxies is a mixture of dust at different temperatures, and attempting to model these with a black-body curve at a single temperature biases the inferred properties of the cooler dust component (e.g. Juvela & Ysard 2012; Hunt et al. 2015). This effect is enhanced in the presence of an AGN, since it is able to heat dust at temperatures typically corresponding to the near-to-mid-IR regime, and with some evidence of FIR emission (e.g. Dicken et al. 2009; Mullaney et al. 2011; Siebenmorgen et al. 2015; Symeonidis 2017; Bernhard et al. 2021, Dicken et al. subm.).

To fit our IR SEDs we tested several models. Our first model is a single modified black-body curve, for which T and β were free to change (see leftmost panels in Fig 1). In fact, these models are still used in the literature to fit galaxy IR SEDs, probably due to their simplicity (e.g. Clements et al. 2018). Our second model was a combination of two modified black-body curves, defined with two dust temperatures and beta indices ($T_{\rm cold}$, $\beta_{\rm cold}$ and $T_{\rm warm}$, $\beta_{\rm warm}$ for the cold and

the warm dust, respectively; see central panels in Fig 1). All of these parameters were free to change. Our third model consisted of two modified black-body curves, with temperatures $T_{\rm cold}$ and $T_{\rm warm}$, but with $\beta_{\rm cold} = 2$ fixed, which is a common value adopted in studies of galaxies (e.g. Dunne & Eales 2001; Vlahakis et al. 2005; Smith et al. 2012; Cortese et al. 2014, see rightmost panels in Fig 1). Therefore, we had in total three different models for the IR emission of our galaxies, two of which used a combination of two modified black-body curves at different temperatures (see Fig. 1).

We performed maximum likelihood estimation (MLE) to optimise the free parameters of each of these models, and fit the SEDs. We used MLE as it allowed us to easily consider upper limits and errors on the fluxes in a self-consistent way (e.g. Bernhard et al. 2019; Grimmett et al. 2019). Due to the complexity of our likelihood function, it could not be maximised analytically. Instead, we maximised it by randomly sampling the posterior distributions of our free parameters, employing the affine invariant ensemble sampler of Goodman & Weare (2010), fully implemented into EMCEE[12] (Foreman-Mackey et al. 2013). The benefit was that we obtained best fitting values with meaningful uncertainties that fully accounted for the presence of upper limits. The median values of the posterior distributions were taken as best fit parameters. Their 1σ uncertainties were estimated by using the standard deviations of the posterior distributions, taking into account the covariance between different parameters (e.g. the $T_{\rm cold}$-$\beta_{\rm cold}$ anti-correlation, in particular).

To reach convergence faster and avoid degeneracies, we reduced the parameter space to physically meaningful values. To do this, we used bounded, normally-distributed priors for each of the parameters defining our models. The priors were such that the explored parameter space was largely consistent with parameters reported in studies of star-forming galaxies (e.g. Hunt et al. 2015; Orellana et al. 2017), as well as those including AGN contributions (e.g. Tadhunter et al. 2014). While attempting to fit the IR SEDs of our samples of ULIRGs and non-AGN elliptical galaxies with our two-component models, we found some degeneracies when considering the warmer and colder β indices independently. Therefore, we assumed $\beta_{\rm cold} = \beta_{\rm warm}$ when fitting these samples, since both Rayleigh-Jeans tails of the warmer and cooler dust contributions are expected to arise from star formation. In contrast, $\beta_{\rm cold}$ and $\beta_{\rm warm}$ were kept independent while fitting the IR SEDs of radio-loud AGNs and radio-quiet QSOs to account for potential differences of the dust properties between those of extended star-forming regions and those of the compact nuclear regions (e.g. Siebenmorgen et al. 2015).

We show in Fig. 1 example SED fits for one object in each of our populations of galaxies, and fit with each of our three models for the dust emission.[13] When using our model with a single black-body curve (see leftmost panels in Fig. 1), we treated the fluxes at $\lambda < 60$ μm as upper limits since the model was not designed to represent the full IR emission of galaxies, where the contribution of the warmer dust can be significant at shorter IR wavelengths. The mean $\beta_{\rm cold}$ and

---

[11] We stress that we use the 160 μm flux, since 160 μm is the longest wavelength with a measured flux available for most of our objects, most of which lack SPIRE measurements.

[12] EMCEE is publicly available at `http://dfm.io/emcee/current/`
[13] The full sets of SEDs and best fitting parameters are available in the online material.
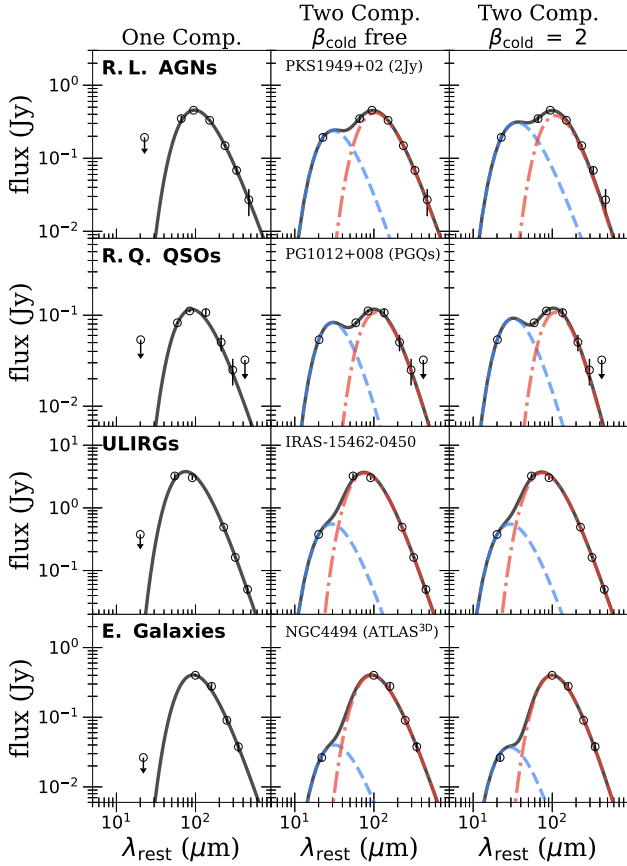
Figure 1. Examples of SED fits for one objects of each of our populations of galaxies. From top-to-bottom, these are radio-loud AGNs, radio-quiet QSOs, ULIRGs, and non-AGN elliptical galaxies, as indicated in the top-left corner of each of the leftmost panels. The names of the sources and their respective samples selected to illustrate our SED fits are indicated at the top of each of the central panels. From left-to-right, the panels correspond to each of our three different models for the dust emission as described in § 3.1.1. The observed fluxes are shown with open circles, and the best SED fits with a continuous black line. Downward arrows indicate upper limits on the fluxes. The warmer and the colder dust contributions are shown with a dashed blue line, and a dot-dashed red line, respectively, for corresponding models.[13]

T_{cold} values and typical range of each of our samples and models are listed in Table 2.

3.1.2 Results of the detailed fits

We first note that each of our three models provide a good fit to the IR SEDs of our samples, whether hosting an AGN or not (see Fig. 1 and online material). Consistent with previous work (see Galliano et al. 2018 for a review), we find that employing a single modified black-body curve generally leads to higher temperatures, and lower β indices for the cooler dust, when compared to employing two modified black-body curves (see Table 2). We note, however, that this is not true for our sample of non-AGN elliptical galaxies, where no differences are found for the mean β indices and temperatures of the two models. In fact, elliptical galaxies are likely to contain less warmer dust (i.e. evolved galax-

ies with lower star formation), when compared to our other samples. Therefore, they are equally well represented by a single black-body curve. We also find that the differences on the mean parameters for the cooler dust, between the one and two-component black body models for the ULIRGs, are less significant, when compared to those found for our samples of AGNs (see Table 2). This is likely related to the presence of a hotter, more prevalent, AGN-heated dust contribution in the latter.

For our models with two modified black bodies, fixing $\beta_{cold} = 2$ leads to mean T_{cold} values that are systematically reduced by $\sim$2-to-6 K, when compared to models with β_{cold} unconstrained. We further note that, when unconstrained, our β_{cold} indices are systematically lower than the value of 2, which is the value often used in studies of galaxies (see Table 2). Overall, the ranges of mean T_{cold} (i.e. $\sim$25–40 K) and β_{cold} (i.e. $\sim$1.4–1.9) values found for our model with two black body components are consistent with those reported in studies of star-forming galaxies (e.g. Hunt et al. 2015; Orellana et al. 2017).

For the remainder of this paper, we exclude our model with a single modified black body curve since it is prone to biases arising from the presence of a warmer dust contribution in some of our samples. Furthermore, since that the typical β_{cold} and T_{cold} of galaxies are generally difficult to estimate due to a degeneracy observed between these two parameters (e.g. Shetty et al. 2009; Juvela & Ysard 2012; Lamperti et al. 2019), we kept our model with two modified black body curves with β unconstrained, as well as that with β fixed to a value of 2.

To calculate the cool dust masses for each object that could be fit, we directly measured $B_\nu(160, T)$ and S_{160} from the fits of the cool dust component, and then used Eq. 1. These values of M_{dust} measured from the SED fits (using $\kappa_{160} = 1.038$ m^2 kg^{-1}), and for each of our models with two modified black body curves are listed in Tables in the online material. The uncertainties on these values of M_{dust} were measured by propagating through Eq. 1 the uncertainties on each of the best fitting parameters, in turn estimated from the posterior distributions, as explained in § 3.1.1.

3.2 The dust masses from flux ratios

Because dust masses for the majority of our galaxies could not be measured using detailed SED fits due to a paucity of data, especially at the longer FIR wavelengths, we developed a method described in § 3.2.1 to measure M_{dust} which requires fewer FIR photometric measurements. The dust masses estimated in this way were then compared against literature values, as described in § 3.2.2.

3.2.1 Method

The two parameters that need to be estimated to calculate M_{dust} are the temperature and the β index of the cold dust, using the 100 and 160 μm fluxes only, since they are available for most of our galaxies (see § 2). To do this, we used a similar approach to that presented in Tadhunter et al. (2014). In the latter, a series of black body curves were constructed based on a T–β grid. For objects that were detected at 100, 160, and 250 μm, a typical $\beta = 1.2$ was determined by

Table 2. List of the mean averages and typical ranges for the best fitting parameters for our galaxies with SEDs that could be fit, combined in terms of galaxy populations and samples (rows in Table), and for each of our three models for the emission of the dust, as described in §3.1.1 (columns in Table). The names of the models are "One comp.", "Two comp.", and "Two comp. $\beta_{\rm cold} = 2$", and correspond to our single black-body curve, two-component black-body curve, and two-component black-body curve with $\beta_{\rm cold} = 2$ fixed, respectively. The census for each of the samples is indicated between brackets under the sample names (see also Table 1).

Populations	Samples	One comp.		Two comp.		Two comp. $\beta_{\rm cold} = 2$	
		$\beta_{\rm cold}$	$T_{\rm cold}$ (K)	$\beta_{\rm cold}$	$T_{\rm cold}$ (K)	$\beta_{\rm cold}$	$T_{\rm cold}$ (K)
Radio AGNs	2Jy (8 sources)	1.2 (0.3)	36.9 (4.2)	1.5 (0.2)	32.8 (3.8)	2.0	28.0 (3.7)
	3CR (4 sources)	1.4 (0.6)	29.2 (9.5)	1.7 (0.2)	24.7 (4.8)	2.0	22.7 (4.2)
QSOs	PGQs (9 sources)	0.7 (0.2)	40.9 (4.9)	1.5 (0.2)	27.1 (3.8)	2.0	23.6 (2.9)
	Type-II (12 sources)	0.8 (0.3)	44.6 (6.2)	1.4 (0.2)	30.1 (9.1)	2.0	23.8 (4.8)
ULIRGs	HERUS (14 sources)	1.9 (0.2)	40.2 (4.1)	1.9 (0.2)	38.9 (3.7)	2.0	36.6 (4.6)
Ellipticals	Atlas[3D] (4 sources)	1.6 (0.2)	28.9 (4.4)	1.6 (0.2)	28.7 (4.7)	2.0	25.3 (3.3)

comparing the observed 100/160 μm and 160/250 μm flux ratios to those predicted by the grid of black body curves. Finally, for all of the sources (i.e. not only those detected at 250 μm), a new series of black body curves was generated with fixed $\beta = 1.2$, and T was chosen to best match the observed 100/160 μm flux ratio of each object.

For this work, we benefited from our SED fits to estimate the β indices, instead of relying on the 100/160 μm and 160/250 μm flux ratios, which was the first step in Tadhunter et al. (2014). We first adopted the mean β index of each sample, as reported in Table 2 for our model with $\beta_{\rm cold}$ unconstrained (i.e. $\beta_{\rm cold}$ listed under the "Two Comp." model in Table 2 for each sample). For the HRS sample, we adopted the mean β index of the Atlas[3D] sample, since no galaxies could be selected for detailed SED fits (see §2.4.2). We also estimated dust temperatures and masses separately assuming a fixed $\beta_{\rm cold} = 2$ for all the samples. This allows us to gauge the effect of using different values of the β index on our results.

The dust temperature T was then calculated by minimising models of black body curves with varying T and fixed β indices against the observed 100/160 μm flux ratios, as in Tadhunter et al. (2014). Two sets of temperatures were derived, depending on whether $\beta_{\rm cold}$ was fixed to the mean of the sample as measured from the SED fits, or to a value of 2. In each case, the observed fluxes at 100 μm were used to estimate the overall normalisation. The uncertainties on T and the normalisations were estimated by propagating the uncertainties on the fluxes, as well as on the β indices when not fixed to a value of 2.

For galaxies that were detected only at 100 *or* 160 μm (see Table 1), we had no constraints on the 100/160 μm flux ratios, and the dust temperature could not be calculated as above. Instead, we adopted the mean temperatures and

uncertainties for the relevant sample as found for sources which were detected at both 100 and 160 μm, and therefore for which we could calculate the temperatures from the 100/160 μm flux ratios and their uncertainties. These corresponded to $T = 34.9\pm0.4$, 31.0 ± 0.8, 30.4 ± 0.3, 31.6 ± 0.3, 32.6 ± 0.2, and 24.3 ± 0.7 K, for the 2Jy, 3CR, PGQs, Type-II QSOs, ULIRGs, and ellipticals (i.e. HRS and Atlas[3D] samples), respectively, when adopting the mean β index for each sample, and $T = 30.5\pm0.3$, 28.8 ± 0.7, 27.0 ± 0.2, 27.2 ± 0.2, 31.7 ± 0.2, and 22.3 ± 0.4 K, respectively, when adopting a fixed $\beta = 2$. We note that these mean temperatures are within ~2–5 K of the mean T values found per population in our detailed SED fits (see Table 2). The normalisation of the inferred black body curve and its uncertainty was then calculated based on whichever of the 100 or 160 μm fluxes was detected, and by propagating the uncertainties on the fluxes and the mean parameters.

For sources with upper limits only (see Table 1), the upper limit at 100 μm was used, along with the mean temperature for the relevant sample, and $M_{\rm dust}$ was treated as an upper limit. We recall that for 20 per cent of radio AGNs (in fact all of the upper limits in the 2Jy sample), the fluxes were treated as upper limits to account for potential non-thermal contamination, instead of true non-detections (see §2).

As for the SED fits (see §3.1.2), we measured $B_\nu(160, T)$ and S_{160} from the black-body curves inferred from the 100 and/or 160 μm fluxes and their ratio alone. The values of $M_{\rm dust}$ measured from the flux ratios (using $\kappa_{160} = 1.038$ m^2 kg^{-1}), assuming $\beta_{\rm cold}$ fixed to the mean of the sample, or $\beta_{\rm cold}$ fixed to a value of 2, are listed in Tables in the online material. The uncertainties on the values of $M_{\rm dust}$ were estimated by propagating through Eq. 1 the uncertainties found on each of the parameters.
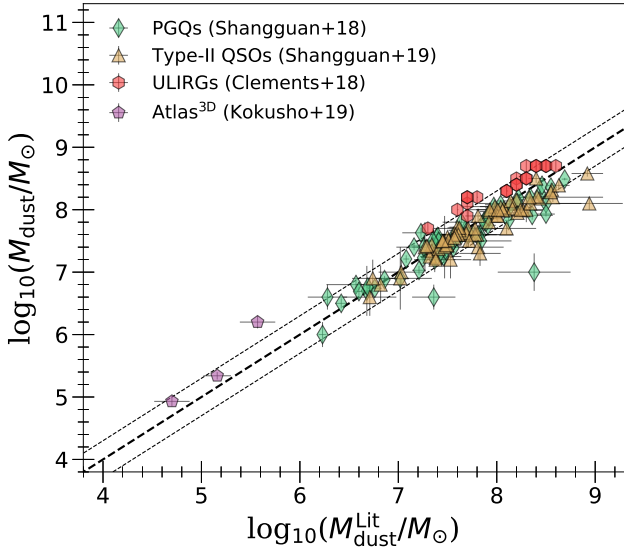
Figure 2. Comparison between our dust masses inferred from the $100/160~\mu$m flux ratios (ordinate), and $M_{\rm dust}^{\rm Lit}$, found in the literature, for the PGQs (Shangguan et al. 2018), Type-II QSOs (Shangguan & Ho 2019), ULIRGs (Clements et al. 2018), and the Atlas$^{\rm 3D}$ (Kokusho et al. 2019) samples (see keys). In each case $\beta_{\rm cold}$ was chosen to best match the adopted method of the corresponding archival studies (see text). The thick and the thin dashed lines show unity, and a factor of two deviation form the latter, respectively.

By comparing the dust masses measured from detailed, two-component SED fits with unconstrained β indices against those measured based on the $100/160~\mu$m flux ratios, where β was fixed to the mean of the sample, we found that the flux ratio method is accurate to within a factor of two-to-five. By adopting $\beta_{\rm cold} = 2$ for the detailed SED fits as well as for the flux ratios, the agreement between the two methods at calculating $M_{\rm dust}$ is reduced to within a factor of 1.2-to-2.5. Moreover, the dust masses for the Type-II QSOs, measured using the flux ratios with $\beta_{\rm cold}$ fixed to the mean value (i.e. 1.4; see Table 2), are systematically higher by a factor of 1.2-to-3, compared to when measured using the flux ratios with $\beta_{\rm cold} = 2$ fixed. We used the Type-II QSOs for the latter comparison since they display the largest difference between the mean $\beta_{\rm cold}$ and the value of 2, therefore gauging the largest effect of the β indices when using the flux ratio method to calculate values of $M_{\rm dust}$.

We emphasise that, although there might be systematic uncertainties in the absolute dust masses by up to a factor of five depending on the method (i.e. detailed fits versus ratio method) or β index (i.e. $\beta_{\rm cold} = 2$ versus $\beta_{\rm cold}$ set to the mean for the sample) assumed, this will not affect the comparisons we make for our results, since we adopt a uniform approach – based on the $100/160~\mu$m ratio method with $\beta_{\rm cold} = 2$ – for all our samples.

3.2.2 *Comparison with literature values*

We collected archival values of $M_{\rm dust}$ to compare against those measured from the flux ratios and presented in this work. For this, we only compared objects detected at both 100 *and* 160 μm. For the Atlas$^{\rm 3D}$ sample, we used the $M_{\rm dust}$

estimates reported in Kokusho et al. (2019), measured from IR SED fits assuming $\beta = 2$. For this reason, we compared against our values of $M_{\rm dust}$ calculated assuming $\beta_{\rm cold} = 2$. For the PGQs and the Type-II QSOs, we used the $M_{\rm dust}$ values reported in Shangguan et al. (2018) and Shangguan & Ho (2019), respectively, where the dust masses were measured from SED fits using the full dust emission model of Draine & Li (2007), after removing the AGN contributions. Because Draine & Li (2007) showed that at $\lambda < 500~\mu$m their models were equivalent to a modified black-body curve with $\beta = 2$, we used for comparison our values of $M_{\rm dust}$ with $\beta_{\rm cold} = 2$. Finally, values of $M_{\rm dust}$ for ULIRGs were taken from Clements et al. (2018), calculated via IR SED fits with a single black-body curve, and β set as a free parameter. Therefore, we compared the latter against our $M_{\rm dust}$ estimated based on the flux ratio method with $\beta_{\rm cold}$ set to the mean value returned by our detailed SED fits when β was free to vary (see Table 2). We stress, however, that this value of $\beta_{\rm cold} \sim 1.9$ is close to the value of 2, such as choosing to compare against values of $M_{\rm dust}$ calculated using the flux ratio method with $\beta_{\rm cold} = 2$ would not impact significantly the comparison.

We show in Fig. 2 that our values of $M_{\rm dust}$ (i.e. $\sim 10^{4-9}~M_\odot$) generally agree with literature values to within a factor of two, regardless of the method used. There are, however, few outliers, but which still agree to within a factor of five. The outliers in the AGN samples (i.e. mainly two PGQs; see Fig. 2) can be explained by a larger contribution of AGN IR emission at 100 μm affecting their $100/160~\mu$m flux ratios, as found when fitting their SEDs to measure SFRs (see § 4 for the SFRs).

We further note that the values of $M_{\rm dust}$ for ULIRGs reported in Clements et al. (2018) appear systematically lower by a factor of $\sim$1.5-to-3, when compared to those measured in this work. In Clements et al. (2018), β was found to be 1.7, instead of $\sim$1.9 here, explaining the systematic differences in $M_{\rm dust}$ for ULIRGs. The lower β indices found in Clements et al. (2018) are likely due to the use of a single modified black-body curve, instead of our two-component approach which removes the contribution from the hotter dust (see § 3.1.1). However, we stress that by using a single black-body curve, although our average β index is slightly lower than when using two black-body curves, it remains higher than that found in Clements et al. (2018, see Table 2).

Benefiting from the general agreement between the values of $M_{\rm dust}$ calculated via the $100/160~\mu$m flux ratios using *Herschel* and those presented in the literature for the Atlas$^{\rm 3D}$ sample calculated using AKARI (Kokusho et al. 2019), we expanded our sample of elliptical galaxies using the 32 objects, including upper limits, with dust masses listed in Kokusho et al. (2019) and that were not observed by *Herschel* (see also § 2.4.1). We show in Fig. 3, panel (a), (b), and (c), that the histogram of $M_{\rm dust}$ for these extra sources taken from Kokusho et al. (2019) is fully consistent with those in our *Herschel* samples. Therefore, including these $M_{\rm dust}$ should not bias our results.

In panel (d) of Fig. 3, we show the distribution of $M_{\rm dust}$ for the 45 elliptical galaxies (excluding S0 morphologies) with direct measurements of molecular and atomic gas masses (taken from Young et al. 2011 and Serra et al. 2012, respectively). A typical gas-to-dust ratio of 140 was used to convert gas masses ($M_{\rm gas}$) into dust masses (e.g. Draine &
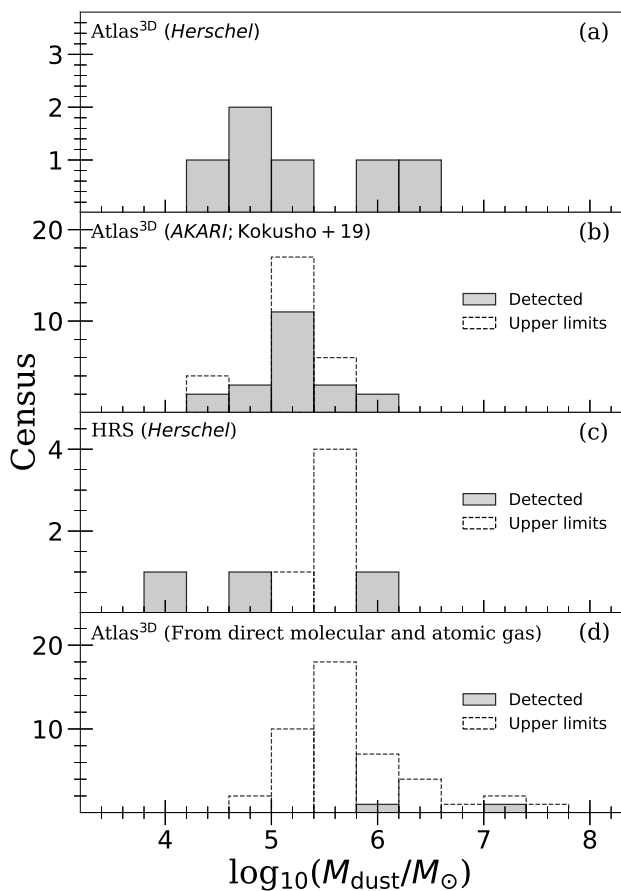
Figure 3. Histogram of M_{dust} for our samples of non-AGN elliptical galaxies. *Panel (a)*: the Atlas^{3D} sample observed with *Herschel*. *Panel (b)*: the Atlas^{3D} sample observed by AKARI (Kokusho et al. 2019). *Panel (c)*: the HRS sample observed with *Herschel. Panel (d)*: the Atlas^{3D} sample with M_{dust} converted from direct measurements of molecular (from Young et al. 2011) and atomic (from Serra et al. 2012) gas masses. We used a factor of 140 to convert direct measurements of M_{gas} into M_{dust} (see text). Each bin is 0.4 dex wide, and the filled bars show the number of objects with measured M_{dust}, while the dashed, open bars show the number of any additional objects with upper limits found in each bin.

Li 2007; Parkin et al. 2012). We stress that the gas-to-dust ratio is highly uncertain (e.g. Kokusho et al. 2019), and our values of M_{gas} are only to be used as a guide. We find that the distribution of M_{dust}, converted from direct measurements of M_{gas}, is consistent with that measured from IR observations, although most of the former is constrained by upper limits only.

Since that the mean stellar masses of elliptical galaxies in the Atlas^{3D} sample is lower than in the radio galaxy hosts (see § 5 and § 7.5), there might be a concern that the comparison is not fair if the dust mass increases with stellar mass. However, there is no evidence for an increase in dust and cool ISM masses with stellar mass for elliptical galaxies (e.g. Young et al. 2011; Kokusho et al. 2019; Davis et al. 2019).

4   MEASURING STAR FORMATION RATES

In addition to the cool ISM content, we aim to compare the star-forming properties of powerful radio AGNs against our comparison samples. The SFRs of our populations of AGNs and galaxies were obtained using IRAGNSEP[14], which decomposes the IR SEDs of galaxies into an AGN and a galaxy contribution, therefore returning SFRs free of AGN contamination (see Bernhard et al. 2021, for details on IRAGNSEP). However, we first modified IRAGNSEP so that it could fit IR SEDs with FIR fluxes (i.e. $\lambda > 100\ \mu$m) constrained by upper limits alone. This was useful for objects which were potentially dominated by non-thermal emission, for which we treated the fluxes as upper limits (see § 2). For these, returned SFRs were also regarded as upper limits. In addition, we added the possibility to fit SEDs with no MIR data (i.e. $\lambda < 70\ \mu$m), for which the AGN templates were not included, since they were impossible to constrain without MIR data. This was useful for objects without reliable *WISE* or *Spitzer*–MIPS fluxes. These SFRs were also regarded as upper limits, since no AGN contributions could be estimated.

For the sample of ULIRGs we set the silicate absorption parameter of IRAGNSEP between $S_{9.7} = 3 - 5$, as most ULIRGs show evidence of strong silicate absorption at 9.7 μm (e.g. Rieke et al. 2009). Assuming the optical-to-IR extinction curve of Draine & Li (2007), these values of $S_{9.7}$ translate to $A_V \sim 43 - 72$ mag, which are consistent with the typical values measured in star-bursting galaxies (e.g. Genzel et al. 1998; Siebenmorgen & Krügel 2007). We stress that ignoring extinction did not change the values of SFRs significantly, but the quality of the fits was generally better once extinction was accounted for. We did not need to do this for our samples of AGNs, since the AGN emission in the MIR often dilutes the strong silicate absorption.

For each IR SED, IRAGNSEP fit a possible combination of 21 models (i.e. 7 different templates for galaxy emission and 2 templates for AGNs), 14 of which contain a template for the IR emission of AGNs. Each of these 21 fits are weighted using the Akaike Information Criterion (e.g. Akaike 1973, 1994, ; AIC), which allows the comparison of models with a different number of degrees of freedom (i.e. those including an AGN contribution against those that do not). The best model has the highest weight (see Bernhard et al. 2021, for more details). To account for the fact that there is no true model, our SFRs were calculated using a weighted sum of all of the 21 possible fits, the weights of which corresponded to the Akaike weights. To estimate realistic uncertainties on the SFRs, in addition to those returned for each of the 21 fits (weighted by their AIC), we included the standard deviation of all the of 21 possible SFRs returned by the fits and weighted by their AIC. The SFRs and upper limits returned by IRAGNSEP for individual objects are listed in Tables available in the online material.

5   MEASURING STELLAR MASSES

To place our samples of AGNs and galaxies in the context of the main sequence of star-forming galaxies (MS), we further

---

[14] IRAGNSEP is freely available at https://pypi.org/project/iragnsep/. Version 7.3.2 has been used in this work.

require stellar masses (M_*). For our samples of radio-loud AGNs and non-AGN elliptical galaxies, reliable values of M_* can be estimated from converting the K_S-band luminosities of the Two Micron All-Sky Survey (2MASS; Skrutskie et al. 2006) using the colour-dependent mass-to-light ratios of Bell et al. (2003). We adopted a $B - V$ colour of 0.95, which is typical of local elliptical galaxies (e.g. Smith & Heckman 1989), and assumed a Chabrier (2003) initial mass function.

For 30 (65 per cent) of the radio AGNs in the 2Jy sample, we used the K-band magnitudes[15] provided in Table 4 of Inskip et al. (2010), where the contribution from point sources (i.e. AGN) have been removed. This was done by decomposing images from the ESO New Technology Telescope (NTT), the United Kingdom Infra-Red Telescope (UKIRT), and the Very Large Telescope (VLT) facilities (see Inskip et al. 2010 for details on the observations and method). For one object (i.e. PKS 0039-44), we used the K-band magnitude provided in Table 3 of Inskip et al. (2010), as it was too faint to model and remove the point source. The latter paper also suggests that the K-band magnitude of PKS 0039-44 was not contaminated by AGN emission, and reflects the stellar emission of the host galaxy. An extra five objects in the 2Jy sample had archival Visible and Infrared Survey Telescope for Astronomy (VISTA) K-band magnitudes, and the redshift of one 2Jy source (i.e. PKS 0117-15) was such that the *WISE* magnitude at 3.5 μm could be converted to a K_S-band magnitude.

For the remaining sources in the 2Jy sample, as well as for the 3CR, HRS and Atlas[3D] objects, we collected archival 2MASS K_S-band magnitudes from the IRSA database. Due to the local nature of our samples, most of our sources will be spatially extended. Therefore, we primarily used extended estimates of the K_S-band magnitudes (Jarrett et al. 2000). These were available for five of the remaining 2Jy objects, 26 (58 per cent) of the 3CR sources, and all of the HRS and Atlas[3D] galaxies. For the rest of the 2Jy and 3CR sources (i.e. two and 16 objects, respectively), we used the 2MASS point source estimate of the K_S-band magnitudes (Skrutskie et al. 2006). We estimated and corrected for the potential missed extended flux by fitting a linear relationship between the extended and the point source magnitudes, calibrated using galaxies that had both measurements available (see Pierce et al. 2021).

While the majority of our K-band magnitudes for the 2Jy sample were corrected for potential AGN contributions, it is possible that those that were not, as well as those in the 3CR sample, suffer significant contamination by AGN emission, therefore biasing measurements of M_*. We found six and 13 sources in the 2Jy and 3CR samples, respectively, that were not corrected for AGN contributions, and that were also previously reported with Type-I AGN emission. The M_* values for these objects were regarded as upper limits. Finally, all of our K-band magnitudes have been corrected for interstellar extinction, and K-corrected using the prescription of Bell et al. (2003), prior to calculating M_*.

The values of M_* and upper limits are listed in Tables available in the online material.

For the PGQs, we used the M_* values provided in Zhang et al. (2016). These were calculated by employing the same M/L method of Bell et al. (2003), adapted for disk galaxies, when necessary, and after decomposing high-resolution optical-to-near IR images (see §3 in Zhang et al. 2016 for more details). We found direct measurements of M_* for 60 per cent of our full sample of PGQs. For the full sample of Type-II QSOs, we used the M_* values provided in Shangguan & Ho (2019), derived from J-band photometry, and using the M/L ratio of Bell & de Jong (2001), constrained by a $B - I$ colour typical of obscured QSOs (see §3.1 in Shangguan & Ho 2019 for more details). Finally, we found stellar masses for 10 ULIRGs in Rodríguez-Zaurín et al. (2010), based on spectral synthesis modelling, and of one ULIRG in the SDSS database.

6 RESULTS

In this section, we compare the dust masses (§6.1) and star-forming properties (§6.2) of our samples of powerful radio AGNs to those of our comparison samples to investigate possible differences in triggering mechanisms.

6.1 The dust content of radio AGNs

We show in Fig. 4 the histograms of $M_{\rm dust}$, split in terms of samples, and where each histogram has been normalised to show the probability density function (PDF). The median and typical range of $M_{\rm dust}$ for each population cannot be directly derived from the PDFs due to the presence of upper limits. Instead, we modelled the observed PDFs, assuming that the distributions of $M_{\rm dust}$ are log-normal with parameters μ (the median $M_{\rm dust}$) and $\sigma_{\rm d}$[16] (the standard deviation of the distribution). We used MLE to optimise μ and $\sigma_{\rm d}$ against the observed PDFs, including upper limits on $M_{\rm dust}$ and EMCEE to explore the parameter space (see also §3.1.1). The μ and $\sigma_{\rm d}$ of each sample, as well as their uncertainties, measured from their posterior distributions, are listed in Table 3. These parameters and the best fit PDFs are also shown in Fig. 4.

The median dust mass of SLRGs in the 2Jy sample appears higher by a factor of 2.5 when compared to that of SLRGs in the 3CR sample (see Fig. 4 and Table 3). However, this is only at the $\sim 1.8\sigma$ level, as calculated from the $M_{\rm dust}$ medians and their uncertainties (Table 3), suggesting that the median $M_{\rm dust}$ values of SLRGs are consistent between the 2Jy and 3CR samples. The discrepancy between the two is likely due to the effects of upper limits on the distributions, since the natures of these upper limits differ between the two samples. While those of the 3CR are mostly from non-detections, which affect the faintest sources, those of the 2Jy are from non-thermal contamination, which, if arising from beaming/orientation effects (e.g. Urry & Padovani 1995), should affect a random sample of objects in the full

---

[15] We note that, strictly speaking, the K_S-band has been used to calibrate the mass-to-light ratio in Bell et al. (2003). When using the K-band magnitudes instead, we did not apply any corrections since these were found negligible compared to the typical uncertainties found for M_*.

[16] We used the subscript "d" for the standard deviations of the distributions to avoid confusion with σ, reserved to indicate the level of significance.

Table 3. List of the median values (μ) and standard deviations (σ_d) for M_dust and SFRs returned by the fits of the observed PDFs (see §6.1 and §6.2). We split between populations, sub-populations, and sub-samples of galaxies. In this table, "RL", "RQ", and "Gal. dom." refer to radio loud, radio quiet, and galaxy dominated, respectively. The numbers between brackets correspond to the estimated 1σ uncertainties derived from the posterior distributions of each of the optimised parameters.

Populations	sub-pop.	sub-samp.	$\mu\left(\log_{10}(\frac{M_\mathrm{dust}}{M_\odot})\right)$	$\sigma_\mathrm{d}\left(\log_{10}(\frac{M_\mathrm{dust}}{M_\odot})\right)$	$\mu\left(\log_{10}\left(\frac{\mathrm{SFR}}{M_\odot/\mathrm{yr}}\right)\right)$	$\sigma_\mathrm{d}\left(\log_{10}\left(\frac{\mathrm{SFR}}{M_\odot/\mathrm{yr}}\right)\right)$
RL AGNs	SLRGs	2Jy	7.30 (0.10)	0.70 (0.10)	0.70 (0.20)	0.80 (0.10)
		3CR	6.90 (0.20)	0.70 (0.10)	0.00 (0.30)	1.20 (0.30)
	WLRGs	FRI	4.00 (1.00)	4.00 (2.00)	-1.00 (1.00)	2.00 (1.00)
		FRII	6.60 (0.30)	0.90 (0.30)	-0.30 (0.30)	0.90 (0.30)
RQ QSOs	–/–	Type-I	7.45 (0.07)	0.55 (0.05)	0.30 (0.10)	0.80 (0.09)
		Type-II	7.64 (0.05)	0.47 (0.04)	0.66 (0.08)	0.70 (0.07)
Gal. dom.	ULIRGs	–/–	8.49 (0.05)	0.32 (0.04)	2.04 (0.08)	0.40 (0.06)
	Elliptical		4.99 (0.09)	0.54 (0.07)	-2.60 (0.40)	1.00 (0.40)

distribution. Therefore, the median M_dust value of SLRGs in the 3CR sample appears reduced to accommodate the larger number of upper limits close to the lower bound of the full distribution, when compared to the 2Jy sample.

We find a median dust mass of $M_\mathrm{dust} = 2 \times 10^7\ M_\odot$, with dust masses covering a range of $10^6 \leq M_\mathrm{dust} \leq 10^9\ M_\odot$ for the SLRGs in the 2Jy sample. The median value is a factor of two higher than that reported in Tadhunter et al. (2014) for the same sample. However, in the latter, a β index of 1.2 was used instead of 2 in this work, and the difference in the median dust masses is fully consistent with that expected from such a difference in the β indices (see §3.2.1).

We further find that the median M_dust value for WLRGs (combining the 2Jy and 3CR samples to overcome low statistics), is lower by a factor of $\sim$2000(3.3σ, hereafter the level of significance are indicated in brackets) and $\sim$5(2.2σ) for those associated with FRI-like and FRII-like radio jets, respectively, when compared to SLRGs in the 2Jy sample (see Fig. 4 and Table 3). Therefore, it appears that the median M_dust value of WLRGs/FRIIs is in better agreement with that of SLRGs in the 2Jy sample, when compared to WLRGs/FRIs. However, we note that these are based on a large number of upper limits (i.e. 60 and 50 per cent upper limits for the WLRG/FRIs and WLRG/FRIIs, respectively) increasing the statistical uncertainties on their median M_dust.

To further test the differences on the average values of M_dust between SLRGs and WLRGs, we focused on the 2Jy sample, since it is not affected by upper limits due to non-detections (see §2.1.1). To do this, we first removed the SLRGs that are potentially contaminated by non-thermal emission (i.e. removing the upper limits on M_dust), and were left with 27 objects out of the 35 SLRGs in the 2Jy sample. Their mean M_dust can be directly calculated, since no upper limits are left, and we found $\log_{10}(M_\mathrm{dust}/M_\odot) = 7.5 \pm 0.1$, which is in agreement with the median value of their full M_dust distribution, including upper limits (see Table 3). We then also calculated the direct mean dust masses (i.e. not using the fits of their PDFs) of WLRG/FRIs and WLRG/FRIIs, including those contaminated by non-thermal emission. Since any non-thermal contamination will boost the FIR fluxes and, therefore, the calculated dust masses, these means are likely to represent up-

per limits on the true mean dust masses. Out of the 11 WL-RGs in the 2Jy sample, we have 6 FRIs and 5 FRIIs, of which 5 and 1 objects are potentially contaminated by non-thermal emission, respectively. The upper limits on their mean M_dust were found to be $\log_{10}(M_\mathrm{dust}/M_\odot) = 6.0 \pm 0.5$ and $\log_{10}(M_\mathrm{dust}/M_\odot) = 7.1 \pm 0.8$ for the WLRG/FRIs and WLRG/FRIIs, respectively. Finally, we compared the mean dust mass of SLRGs (that obtained after removing the upper limits) to that of WLRGs, therefore calculating a *lower limit* on the differences, which constitutes a conservative approach. By doing this, we find that the mean dust masses of WLRG/FRIs and WLRG/FRIIs are lower by factors of *at least* $\sim$30(3σ) and $\sim$3(<1σ) when compared to that of the SLRGs in the 2Jy sample. Therefore, at least in the 2Jy sample, and in agreement with the results of the PDF fits, it appears that the mean dust mass of WLRG/FRIs is lower when compared to that of SLRGs. In contrast, we find no clear differences in the mean dust masses of WLRG/FRIIs and SLRGs in the 2Jy sample.

Furthermore, we do not find any significant differences between the median M_dust of SLRGs in the 2Jy sample, as measured from the fits of their PDFs, and those of Type-I QSOs (difference at $\sim 1.6\sigma$ level). By contrast, we find that the median M_dust of SLRGs in the 2Jy sample is *significantly* lower by a factor of $\sim$2.2(3σ) when compared to Type-II QSOs. However, we note that, when considering the sub-sample of SLRGs in the 2Jy sample with $L_\mathrm{[OIII]} > 4.2 \times 10^{34}$ W, which is the lowest $L_\mathrm{[OIII]}$ luminosity in our Type-II QSO sample, the difference is less significant (difference at 2.1σ level). Our median values of M_dust for Type-I and Type-II QSOs are also in excellent agreement with those reported in Shangguan & Ho (2019), and no significant differences are found between the median M_dust of these two classes (difference at $\sim 2.2\sigma$ level).

Finally, using the medians from the fits to the PDFs, we find that the median M_dust of SLRGs in the 2Jy sample and that of WLRG/FRIIs in the 2Jy and 3CR samples are enhanced by factors of $\sim$200(17σ) and $\sim$40(5σ), respectively, when compared to those of non-AGN classical elliptical galaxies. In contrast, the median M_dust of WLRG/FRIs (although weakly constrained) is consistent with that of non-AGN elliptical galaxies (difference at $\sim 1\sigma$ level). We note that the PDFs of the latter have been built by combin-
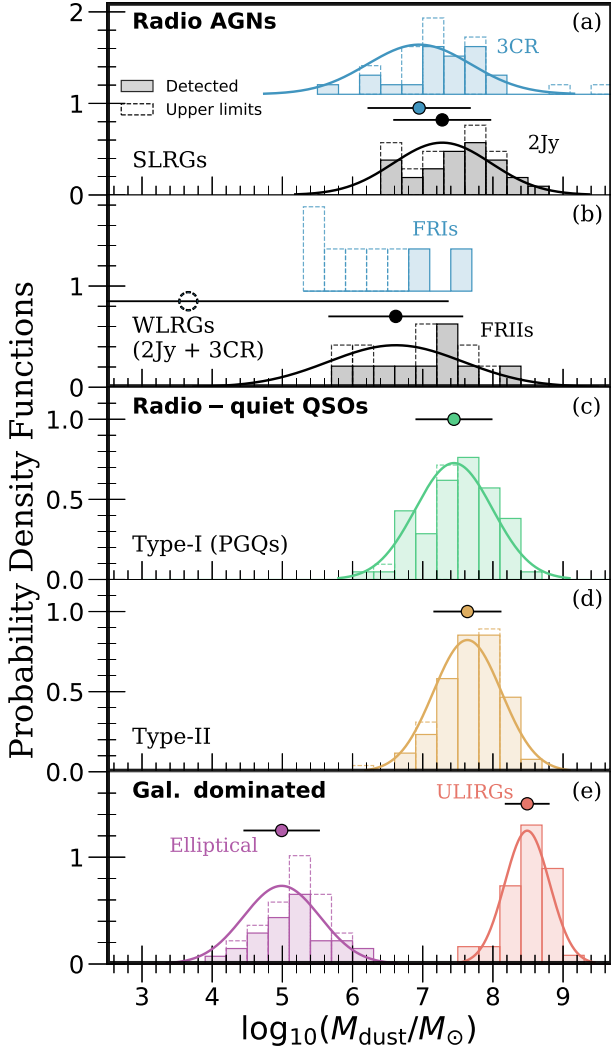
Figure 4. The distributions of $M_{\rm dust}$ for each of our populations and sub-samples of galaxies. Panels (a) and (b) are for radio AGNs, split in terms of SLRGs – panel (a) – and WLRGs – panel (b). We further sub-divided the SLRGs into the 2Jy and 3CR samples, and the WLRGs (combining the 2Jy and 3CR samples) into FRIs and FRIIs (these further sub-divisions are shown by offsetting one of the histograms in panels (a) and (b)). Panels (c) and (d) are for radio-quiet QSOs split in terms of Type-I – panel (c) – and Type-II – panel (d) – AGNs. Panel (e) shows the galaxy dominated samples, including the non-AGN classical elliptical galaxies (purple histogram), and the ULIRGs (orange histogram). The histograms show the observed PDFs of $M_{\rm dust}$, where filled bars correspond to the contribution from detected sources, and empty dashed bars from any additional upper limits. The smooth log-normal distributions show the best model PDFs, which account for upper limits. The best fit parameters are shown with colour-filled circles (medians μ) and error bars (uncertainties $\sigma_{\rm d}$) above or below each of their corresponding PDFs. For WLRG/FRIs we do not show the fitted PDF, and we show the average parameters with an open dashed circles since they are mostly constrained by upper limits.
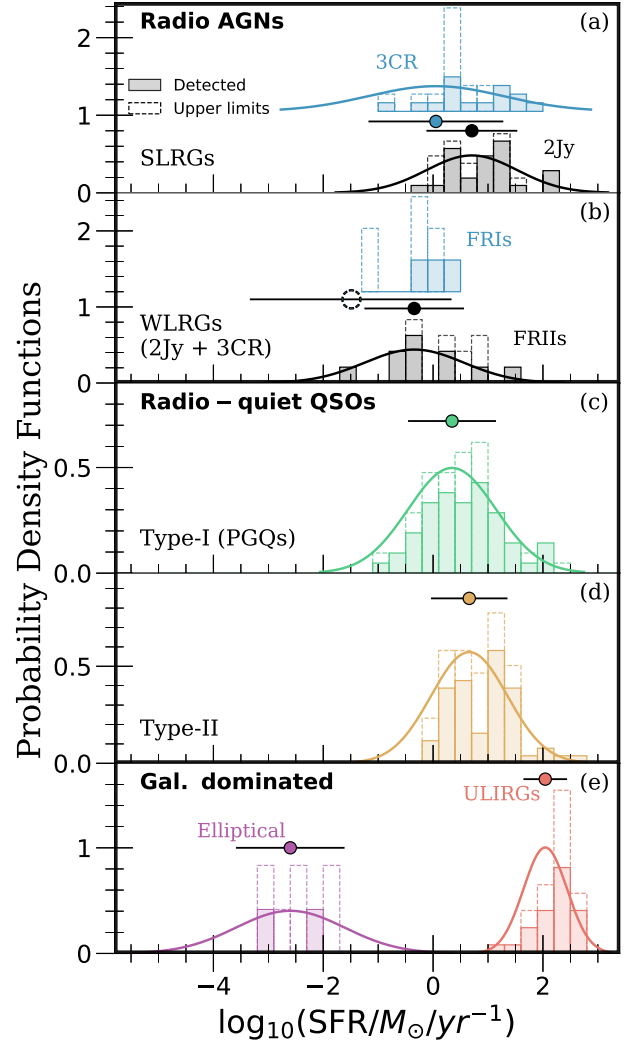
Figure 5. Same as Fig 4, but for the SFRs.

ing the Atlas[3D] and HRS samples with *Herschel* observations, as well as dust masses of elliptical galaxies observed with AKARI taken from Kokusho et al. (2019; see § 3.2.2). It is also striking that these medians are lower by a factor of $\sim$16(11σ), $\sim$31000(5σ), and $\sim$80(6σ), for the SLRGs, WLRG/FRIs, and WLRG/FRIIs, respectively, when compared to that of ULIRGs. These are consistent with early results reported in Tadhunter et al. (2014) for SLRGs only. However, we note that the model PDFs do show some overlap between these populations of galaxies (see Fig. 4).

6.2 The star formation rates of radio AGNs

We show in Fig. 5 the histograms of SFRs, split in terms of galaxy populations and samples. Each histogram has been normalised to show the PDF. As for the distributions of $M_{\rm dust}$, we measured the median SFRs (μ) and standard deviations ($\sigma_{\rm d}$) of each sample by fitting log-normal distributions to the observed histograms, including upper limits on SFRs (see § 6.1). The resulting statistics are listed in Table 3 and shown in Fig. 5.

We find that the median SFRs of SLRGs in the 2Jy sam-

ple is higher by a factor of $\sim 4(1.7\sigma)$, when compared to that of the SLRGs in the 3CR sample (see Fig. 5 and Table 3). The level of significance suggests that the median SFRs of SLRGs in the two samples are consistent within the uncertainties, especially considering the different effects that the upper limits might have on the two samples (see § 6.1): it is likely that the apparent differences between the two distributions can be attributed to the large number of SFR upper limits for the 3CR sample (i.e. ~ 50 per cent), when compared to the 2Jy sample (i.e. ~ 30 per cent). This acts to reduce the median SFR and increase the typical range of $M_{\rm dust}$ in the 3CR sample, when compared to the 2Jy sample (see Table 3). Adopting the SFRs of SLRGs in the 2Jy sample, since better constrained, the median SFR is $\sim 5\ M_\odot\ {\rm yr}^{-1}$, and the values span the range 0.3–$300\ M_\odot\ {\rm yr}^{-1}$.

We further find that the median SFR of WLRGs (combining the 2Jy and 3CR samples to overcome low statistics) is lower by factors of $\sim 50(1.7\sigma)$ and $\sim 10(2.8\sigma)$ for those associated with FRI-like and FRII-like radio jets, respectively, when compared to SLRGs in the 2Jy sample (see Fig. 5 and Table 3). Because of the potential effects of upper limits, we performed a similar analysis to that presented in § 6.1 for the dust masses, allowing us to derive a conservative difference between the median SFRs of SLRGs and WLRGs in the 2Jy sample. In doing this, we found that the median SFRs of WLRG/FRIs and WLRG/FRIIs in the 2Jy sample are lower by factors of *at least* $\sim 30(7\sigma)$ and $\sim 6(2\sigma)$, respectively, when compared to the median SFR of SLRGs in the 2Jy sample. Consistent with our results on the median dust masses of these populations, the median SFR of WLRG/FRIIs appears to be in better agreement with that of SLRGs, at least in the 2Jy sample, compared to when considering the difference between WLRG/FRIs and SLRGs.

We also find that the SFRs of the SLRGs in the 2Jy sample are fully consistent with those of Type I and Type II radio-quiet QSOs. Furthermore, there are no differences between the PDFs for SFR of Type-I and Type-II QSOs, consistent with previous work (e.g. Shangguan & Ho 2019; Mountrichas et al. 2021).

Finally, using the medians from the fits to the PDFs, we find that the median SFRs of SLRGs in the 2Jy sample and that of WLRG/FRIIs in the 2Jy and 3CR samples are enhanced by factors of $\sim 2000(7.4\sigma)$ and $\sim 200(4.6\sigma)$, respectively, when compared to those of non-AGN classical elliptical galaxies. In contrast, although the median SFR of WLRG/FRIs appears weakly constrained, it is lower by a factor of $\sim 40(1.5\sigma)$ when compared to non-AGN elliptical galaxies. On the other hand, these median values are lower by factors of $\sim 20(6.2\sigma)$, $1100(3\sigma)$, and $\sim 200(7.5\sigma)$, for the SLRGs, WLRG/FRIs, and WLRG/FRIIs, respectively, when compared to that of ULIRGs. This follows a similar pattern to the results reported for the dust masses of radio AGNs in § 6.1. However, it is important to add the caveat that the dust masses and SFRs are not entirely independent, since they have both been calculated using the FIR luminosities.

7 DISCUSSION

In this section, we explore the implications of the results for our understanding of triggering and feedback in radio AGNs.

In particular, we first discuss whether the cool ISM masses found are sufficient to power QSO-like activity (§ 7.1). Then, in § 7.2 and § 7.3 we explore the triggering mechanisms of AGNs and how they connect to the amount of gas available for both AGN activity and star formation. In § 7.4 we discuss the potential impact of AGN feedback on AGN hosts. Finally, in § 7.5, we place our samples of AGNs in the broader context of the MS of galaxies, and discuss the implications in terms of their triggering mechanisms.

7.1 Sustaining powerful QSO activity

In § 6.1, we established that the dust masses of SLRGs in the 2Jy sample, which are better constrained than those of the 3CR, have a median of $M_{\rm dust} = 2 \times 10^7\ M_\odot$ and span $M_{\rm dust} \sim 10^{6-9}\ M_\odot$. Assuming a typical gas-to-dust ratio of 140 (see § 3.2.2), we find that the median gas mass of SLRGs is $M_{\rm gas} = 2.8 \times 10^9\ M_\odot$ with a range of $M_{\rm gas} \sim 10^{8-11}\ M_\odot$. If we follow the arguments proposed in Tadhunter et al. (2014), assuming QSO bolometric luminosities $L_{\rm bol} > 10^{38}$ W, and a radiative efficiency of 10 per cent, a mass inflow rate of $\dot M > 0.2\ M_\odot\ {\rm yr}^{-1}$ onto the supermassive black-hole is required to sustain QSO activity. Widely varying constraints on the lifetime of QSOs suggest that QSOs are "on" for (i.e. duty cycle) $t_{\rm dc} \sim 10^{6-9}$ yr (e.g. Martini 2004; Adelberger & Steidel 2005; Croom et al. 2005; Shen et al. 2009; White et al. 2012; Conroy & White 2013). Therefore, the total mass accreted onto the black hole during QSO episodes is $M_{\rm acc} > 2 \times 10^{5-8}\ M_\odot$. However, the gas feeding such AGN episode is likely to have originated in a gas reservoir at larger scales; this reservoir will eventually form stars in the bulge of the host galaxy. Indeed, in order to maintain the observed black hole-to-bulge mass relationship, the total mass of the gas reservoir is required to be ~ 500 times larger than the mass of gas accreted by the black hole (e.g. Marconi & Hunt 2003). Therefore, for the black hole to accrete $M_{\rm acc} > 2 \times 10^{5-8}\ M_\odot$ for $t_{\rm dc} \sim 10^{6-9}$ yr, a total reservoir containing $M_{\rm gas}^{\rm tot} \gtrsim 10^{8-11}\ M_\odot$ of gas is required. These estimates of $M_{\rm tot}$ are in remarkable agreement with the range of $M_{\rm gas}$ estimated in this work for SLRGs.

We further found evidence for WLRGs associated with FRI-like radio jets to have a lower median dust mass when compared to that of SLRGs (see § 6.1). The values span the range $M_{\rm dust} \sim 10^{5-8}\ M_\odot$, which translate to $M_{\rm gas} \sim 10^{7-10}\ M_\odot$, respectively. Following the aforementioned argument, these overlap with the gas masses necessary to trigger powerful radiatively-efficient QSOs. Therefore, at least for some of the most gas-rich WLRGs associated with FRIs, the presence of a substantial gas reservoir is not a sufficient condition to trigger a powerful QSO. In this case, other factors such as the detailed distribution and dynamics of the cool ISM are likely to be important (e.g. Tadhunter et al. 2014). In fact, as the cool ISM settles into a dynamically stable configuration post merger, the rate of gas infall to the black hole is expected to drop, leading to a lower level of nuclear activity and perhaps a WLRG AGN classification (see Tadhunter et al. 2011, and references therein).

7.2 The importance of mergers for triggering powerful radio QSOs

We found that the cool ISM masses of SLRGs in the 2Jy sample are enhanced by a factor of $\sim 200 (17\sigma)$, when compared to our sample of non-AGN classical elliptical galaxies (see §6.1 and Table 3). We also recall that the latter is likely to be more FIR bright and dust-rich than typical elliptical galaxies of similar stellar mass in the local universe due to selection effects (see §2.4). Therefore the quoted factor of ~ 200 corresponds to a lower limit. Because powerful radio AGNs mostly reside in elliptical galaxies, there must be some mechanisms at work to enhance the cool ISM masses of the elliptical hosts, which in turns could be connected to the triggering of the AGN. Compelling evidence has been found in deep optical imaging for a high incidence of tidal features and double nuclei, strongly suggesting that galaxy mergers and interactions are important for their triggering (e.g. Ramos Almeida et al. 2011; Ramos Almeida et al. 2012; Pierce et al. 2021). However, the fact that we found that the median M_{dust} and SFR of SLRGs are significantly lower than those of ULIRGs, implies that for most objects the triggering mergers and interactions are likely to have been relatively minor in terms of their cool ISM contents. This is consistent with the evidence that population of massive elliptical galaxies has mainly evolved via minor mergers since $z \sim 1$ (e.g. Bundy et al. 2009; Kaviraj et al. 2009).

Although the majority of SLRGs are unlikely to be triggered at the peaks of major gas-rich galaxy mergers, there is a significant overlap between the values of M_{dust} (and SFRs) for SLRGs and ULIRGs (see Fig. 4 and Fig. 5). To estimate the fraction of SLRGs in our samples that could be triggered by a ULIRG-like major gas-rich merger, we calculated the overlapping fraction between the PDFs of M_{dust} for our samples of SLRGs and ULIRGs (see §6.1, Fig. 4, and Table 3 for the PDFs). We found fractions of 22^{+11}_{-10} per cent and 11^{+8}_{-7} per cent for the SLRGs in the 2Jy and 3CR samples, respectively. Repeating this comparison for the PDFs of SFRs led to similar summary statistics. In addition, we find that 4 out of the 5 SLRGs in the 2Jy sample (80 per cent) with $M_{dust} > 10^8 \ M_\odot$, a value consistent with the typical dust masses measured for ULIRGs, are also reported to have strong poly-aromatic hydrocarbon (PAH) emission at MIR wavelengths, which is a sign of ongoing star formation (Dicken et al. 2012).

Similarly to the SLRGs, we also found that the cool ISM properties of WLRG/FRIIs were significantly enhanced compared to those of classical elliptical galaxies, yet depleted when compared to ULIRGs (see §6.1). In contrast, the cool ISM properties of WLRG/FRIs were not found significantly enhanced when compared to those of classical elliptical galaxies, suggesting that both populations could be consistent in terms of their cool ISM properties. These results could also imply different triggering mechanisms between SLRGs and WLRGs/FRIs, in agreement with previous work (e.g. Hardcastle et al. 2007; Buttiglione et al. 2009; Tadhunter et al. 2011). This is also supported by recent evidence from deep optical imaging that mergers are less important for WLRGs compared to SLRGs (e.g. Ramos Almeida et al. 2011; Pierce et al. 2021). An alternative fuelling scenario for WLRGs involves the direct accretion of the hot ISM (Best et al. 2005; Allen et al. 2006; Best et al. 2006; Hardcas-

tle et al. 2007; Buttiglione et al. 2009), which is possible in our samples of WLRG/FRI since we find a smaller amount of cool ISM when compared to SLRGs. Finally, the similarities found between the cool ISM properties of WLRG/FRIIs and SLRGs is consistent with the idea that the AGNs in the WLRG/FRIIs have recently switched off, and the information has not yet reached the hotspots of the radio lobes (e.g. Buttiglione et al. 2010; Tadhunter et al. 2012).

7.3 The lack of relationship between AGN power and gas mass

In §7.2 we suggested that the differences in the dust masses between SLRGs and WLRG/FRIs relate to them being triggered by different mechanisms. We now investigate whether there is a direct relationship between M_{gas} and $L_{[OIII]}$ for these populations, where $L_{[OIII]}$ can be used to trace AGN bolometric luminosity (e.g. Heckman et al. 2005; Stern & Laor 2012; Dicken et al. 2014). Fig. 6 shows that there is a strong apparent relationship between M_{gas} and $L_{[OIII]}$ across several orders of magnitude in both quantities for SLRGs, WLRGs, and radio-quiet QSOs. However, once split in terms of redshift (over $z \sim 0.01$ to $z \sim 0.7$), we also find a strong relationship with redshift, suggesting that the apparent connection between M_{gas} and $L_{[OIII]}$ is fully driven by redshift (i.e. Malmquist bias). This is consistent with results from Shangguan & Ho (2019), where no relationships were found between M_{gas} and the bolometric luminosities of the PGQs and Type-II QSOs. In an attempt to quantify this, we performed multi-linear regressions between M_{gas}, $L_{[OIII]}$, and z for our samples of SLRGs and WLRGs. We found no relationships between M_{gas} and $L_{[OIII]}$ once redshift was accounted for.

In Fig 6, it also appears that a minimum gas reservoir of $M_{gas} \sim 10^8 \ M_\odot$ is required to trigger radiatively efficient AGNs, as represented by SLRGs and radio-quiet QSOs. However, the lack of a direct relationships between M_{gas} and the power of the AGN, suggests that, although a minimum gas reservoir is likely necessary to trigger the most powerful AGNs, it is not by itself sufficient to explain the range of AGN properties: other factors, such as the gas distribution, extend to which the gas has settled into a stable dynamical configuration, and overall gas dynamics are also likely to be important (see also §7.2).

7.4 AGN power versus star-formation efficiencies: the effect of AGN feedback

In the most recent cosmological simulations, AGN feedback is used to regulate star formation in order to reproduce the local scaling relationships between the black hole and bulge masses, as well as the galaxy mass function (e.g. Schaye et al. 2015). The net effect of such AGN feedback is a suppression of the "in-situ" SFRs, via the heating and/or removal of the cold gas (e.g. Di Matteo et al. 2005; Zubovas & King 2012; Costa et al. 2018). While considerable evidence now exists that AGN drive powerful, multi-phase outflows that are likely to affect the host galaxies *at some level* (see Fabian 2012 for a review), aside from few individual objects (e.g. Nesvadba et al. 2010; Lanz et al. 2016; Nesvadba et al. 2021) the direct impact that these outflows have on SFRs
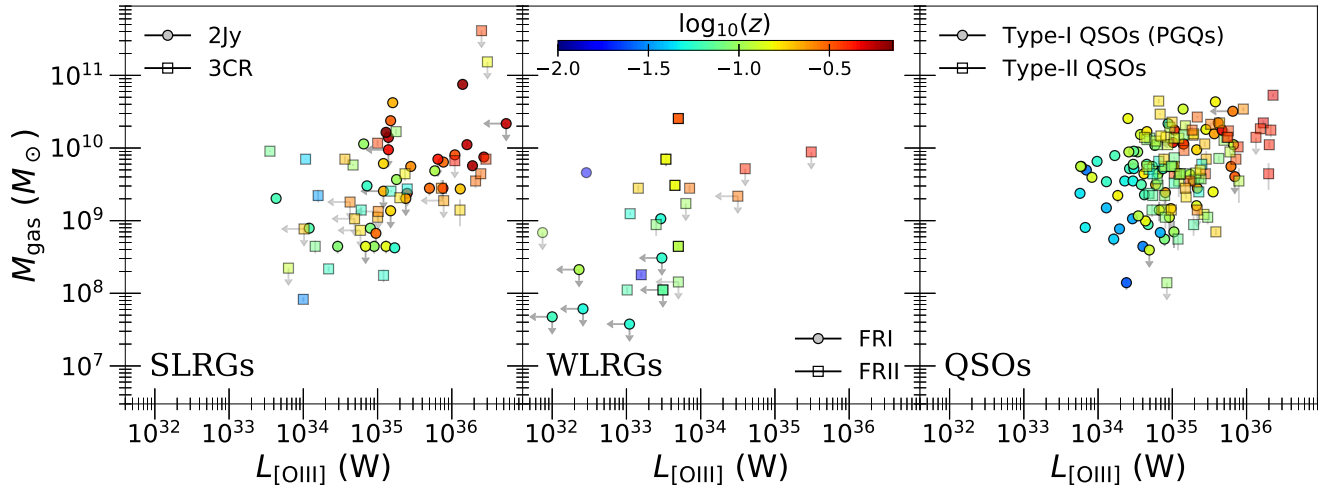
Figure 6. The cool ISM masses of our samples of AGNs versus $L_{[OIII]}$, a proxy of AGN power. In reading order, we have the SLRGs, split in terms of the 2Jy and 3CR samples, the WLRGs, split in terms of FRI and FRII radio morphologies, and the radio-quiet QSOs, split in terms of Type-I (PGQs) and Type-II AGNs. Arrows indicate upper limits. The colour-code indicates redshift, as shown by the colour bar at the top of the central panel ($0.01 < z < 0.7$).
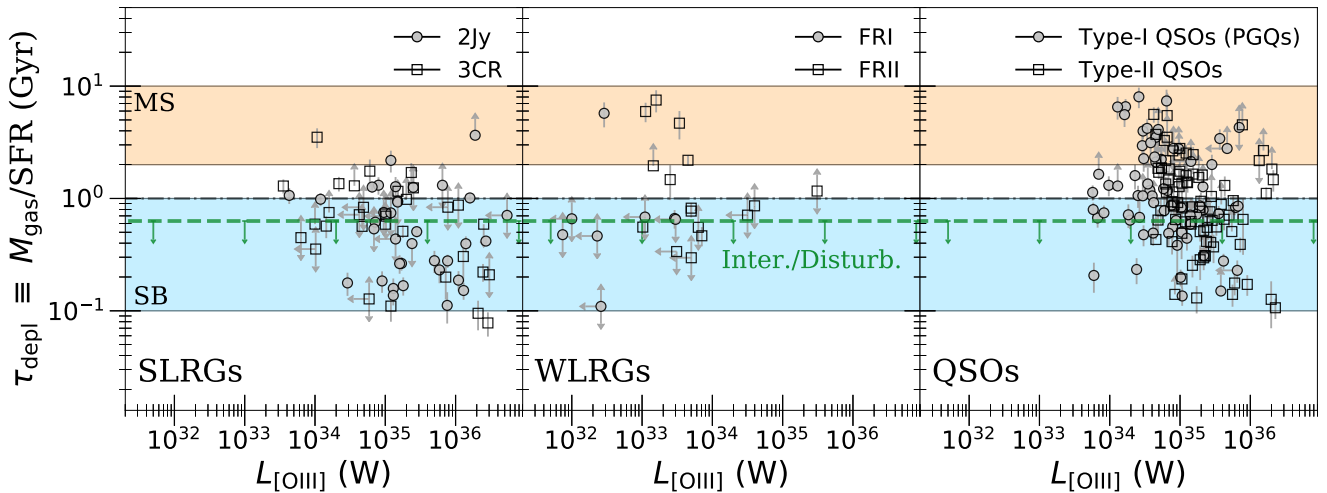

Figure 7. The depletion timescales τ_{depl}, measured as M_{gas}/SFR and expressed in Gyr, versus $L_{[OIII]}$ (or AGN power) for our samples of SLRGs, WLRGs, and radio quiet QSOs (from left-to-right, respectively). We split the SLRGs into the 2Jy and 3CR samples, the WLRGs into FRIs and FRIIs, and the QSOs into Type-Is (PGQs) and Type-IIs (see keys). Arrows indicate upper and lower limits. The filled orange and blue areas indicate the range of τ_{depl} typically observed in star-forming (MS) and star-bursting (SB) galaxies, respectively (Kennicutt 1998). The horizontal dashed green line with downward arrows show the τ_{depl} below which most of interacting galaxies are expected to be found, as taken from Saintonge et al. (2012).

remains uncertain. Indeed, most statistical studies do not find any clear signs of "in-situ" SFR suppression as a consequence of AGN feedback (e.g. Maiolino et al. 1997; Stanley et al. 2015; Rosario et al. 2018; Shangguan et al. 2018; Ellison et al. 2019; Shangguan & Ho 2019; Jarvis et al. 2020; Shangguan et al. 2020; Yesuf & Ho 2020).

To investigate this in our samples of AGNs, we plot in Fig. 7 the depletion timescale τ_{depl}, calculated using M_{gas}/SFR (expressed in Gyr), against $L_{[OIII]}$ for the SLRGs, WLRG/FRIs, WLRG/FRIIs, and radio-quiet QSOs. Note that potential correlations with redshift can be ignored in the case of τ_{depl}, because both the gas masses and SFRs would be affected in a similar way. No clear correlations are

found between τ_{depl}, which represents the inverse of the star formation efficiency, and $L_{[OIII]}$, and there is a considerable scatter in τ_{depl} for most $L_{[OIII]}$ values.

Interestingly, we find that SLRGs mostly show shorter τ_{depl} (i.e. $\lesssim 1$ Gyr), when compared to WLRGs, implying vigorous SFRs for their gas masses (i.e. 5 $M_\odot$ yr^{-1} on average). Roughly half of our radio-quiet QSOs also show such short values of τ_{depl}, which are typically observed in starbursting galaxies, and suggest high star-formation efficiencies where the gas is consumed rapidly (e.g. Kennicutt 1998).

We also show in Fig. 7 with a dashed-green line the mean value of τ_{depl} found for interacting and disturbed nearby galaxies (including major mergers) in the full sam-

ple of the CO Legacy Database for the Galex-Arecibo-SDSS Survey (COLD GASS Saintonge et al. 2011), as reported in Saintonge et al. (2012), and based on molecular gas measurements. We stress that, in the latter, although the majority of interacting systems were found with shorter values of τ_{depl} (i.e. < 1 Gyr), not *all* galaxies in their sample with shorter values of τ_{depl} were interacting systems, and their control sample (i.e. non-interacting systems) spanned a large range of values (i.e. 0.5-to-5 Gyr), largely overlapping with those of interacting systems, but with a mean of ~ 1 Gyr.

We note that the SLRGs in our samples display a heavily skewed distribution toward shorter τ_{depl} values, consistent with those typically measured for interacting systems, suggesting that there is an excess of galaxies in that region, compared to the general population (see Fig. 7). This is consistent with the idea that SLRGs are mainly triggered in interacting systems (see § 7.2). In contrast, the distribution of τ_{depl} for WLRGs and radio-quiet QSOs appears randomly distributed around to the mean value of the full sample of Saintonge et al. (2011; i.e. ~ 1 Gyr). This is consistent with them being triggered in a range of situations, some of which will be connected to a merger, and consistent with the lesser role of mergers in WLRGs when compared to SLRGs.

Overall, we do not find any signs of reduced star-formation efficiencies, which is an expected outcome of AGN feedback. We stress, however, that IR-based SFRs are averaged over ~ 100 million years. Therefore, it is possible that the effect of AGN feedback on the star-formation efficiencies is not yet apparent.

7.5 Powerful radio AGNs: link with the rejuvenation of galaxies

To place our AGN samples in the broader context of galaxy evolution, we now compare the SFRs of our AGN hosts to those expected from the main sequence (MS) of galaxies. This is partly motivated by suggestions that AGN feedback plays an important role in the rapid quenching of galaxies, placing them below the MS (e.g. Smethurst et al. 2016). To test this, we calculated $R_{MS} \equiv \text{SFR/SFR}_{MS}$, where SFR_{MS} is the corresponding MS SFR at a given M_* and redshift. We use the MS of Sargent et al. (2014), who defined a linear relationship between $\log_{10}(\text{SFR})$ and $\log_{10}(M_*)$ for star-forming galaxies. The results are depicted in Fig. 8.

We first note that the elliptical host galaxies of most of our powerful radio-loud AGNs have high stellar masses ($M_* > 10^{11}\,M_\odot$), in contrast to our samples of radio-quiet QSOs which tend to have lower values of M_*, on average. This is in agreement with many past studies on the stellar masses of powerful radio AGNs (e.g. Dunlop et al. 2003; Inskip et al. 2010; Tadhunter et al. 2011). We further find that the values of R_{MS} for powerful radio AGNs are consistent with a large range of values, from those typical of classical elliptical galaxies (i.e. $R_{MS} \sim 0.001$) to those of strongly star-bursting systems (i.e. $R_{MS} \sim 4$), but remain below those of most ULIRGs (i.e. $R_{MS} \sim 10$-100). Interestingly, the majority of powerful radio AGNs are located below the MS of Sargent et al. (2014), at given M_* and redshift. This contrasts with radio-quiet QSOs, that are typically found to be consistent with the MS, in agreement with the results of Shangguan & Ho (2019). The latter authors also reported no
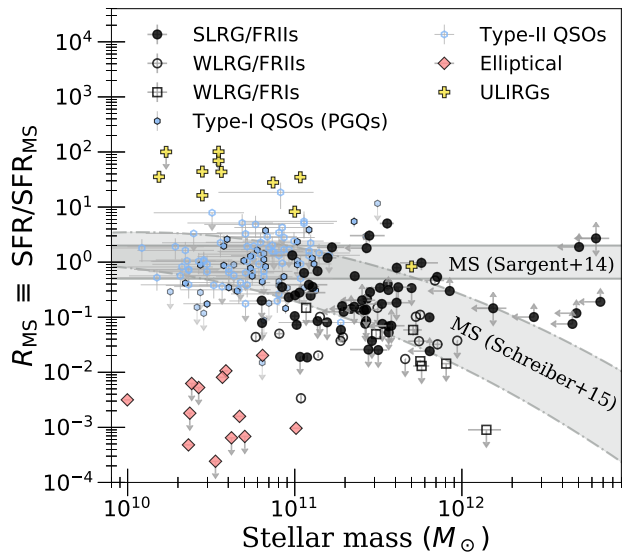

Figure 8. The SFRs relative to that of the MS (R_{MS}) of Sargent et al. (2014) versus M_* for our galaxy populations. We separated radio AGNs into SLRGs, WLRG/FRIs, and WLRG/FRIIs, as well as radio-quiet QSOs into Type-I and Type-II (see keys). Arrows indicate upper and/or lower limits on R_{MS} and M_*. The scatter around the MS of Sargent et al. (2014) is shown with a grey band delimited by continuous lines. The curved grey bands delimited by dot-dashed lines show the deviations of the MS of Schreiber et al. (2015) from that of Sargent et al. (2014), at $0.01 < z < 0.7$, and including the scatter.

This deviation could be due to a population of rejuvenated galaxies and coincides with the R_{MS} of our samples of powerful radio AGNs.

differences in the R_{MS} values between Type-I and Type-II QSOs, as we find here.

It is notable that the SLRGs show a wide range of R_{MS} values. Moreover, while there is an overlap in the distributions, the R_{MS} values of the SLRGs are higher on average than those of WLRGs, particularly the WLRG/FRIs sources whose R_{MS} values all lie well below the MS of Sargent et al. (2014; see Fig. 8). This is consistent with WLRGs having lower SFRs when compared to SLRGs, since they are hosted by galaxies with similar stellar masses at similar redshifts. It is also consistent with the longer depletion timescales found in WLRGs when compared to SLRGs (see § 7.4). Therefore, since at least some WLRGs also appear to have significant cool ISM masses (see § 7.2), it implies that some mechanisms are at work to reduce the efficiency of both AGN activity and star formation in WLRGs. For example, the gas might have settled to a more stable dynamical configuration in the WLRGs (see § 7.1). In this context, we note that there is evidence for reduced star formation efficiencies in early-type galaxies that have accreted gas through minor mergers with gas-rich galaxies (Davis et al. 2015), and for which the gas appears to have reached a relatively dynamically settled state.

One attractive explanation for our finding that radio-loud AGNs tend to fall below the MS, in contrast to radio-quiet QSOs, is that radio jets play a key role in quenching star formation, as expected from some cosmological simulations. However, this picture is inconsistent with the fact that

the majority of SLRGs have relatively high star-formation efficiencies which do not show any signs of deficiency (see § 7.4). Therefore, it is more plausible that we are witnessing the late-time retriggering of galaxies, in terms of star formation and AGN activity (e.g. Tadhunter et al. 2014).

Late-time re-triggering is also supported by the location of our powerful radio AGNs in the R_{MS}-M_* parameter space. In fact, they coincide with a specific type of massive galaxy in the local Universe that are believed to be rejuvenated (i.e. re-triggered), and for which a quenched bulge was formed early on (i.e. typically $z > 2$), followed by a more recent burst of star formation (e.g. Clemens et al. 2009; Thomas et al. 2010; Pandya et al. 2017; Chauke et al. 2019). This has the effect of moving the otherwise quiescent systems toward the MS of galaxies. Such rejuvenation has also been used to explain the apparent curvature in the MS at high stellar masses ($M_* > 10^{11} M_\odot$) that has been found in some studies (e.g. Schreiber et al. 2015): as the (quiescent) galaxy bulges become more dominant at high stellar masses, any star formation due to late-time gas accretion becomes less closely tied to the total stellar mass, so the objects fall further below the MS (e.g. Mancini et al. 2019). The position of the curved MS for star-forming galaxies of Schreiber et al. (2015) for $0.01 < z < 0.7$, relative to the MS of Sargent et al. (2014) is shown in Fig. 8 (including the scatter).[17]

Interestingly, most of our powerful radio-loud AGNs lie on the curve of the MS of Schreiber et al. (2015), where there is significant deviation from the linear MS of Sargent et al. (2014), perhaps due to a population of rejuvenated galaxies (see Fig 8). In contrast, a relatively high proportion of WLRGs fall below the curve of the MS of Schreiber et al. (2015), again emphasising their lower SFRs, which are perhaps related to triggering mechanisms that are different from those of SLRGs (e.g. direct accretion of hot gas from the X-ray haloes). Relative to the curved MS of Schreiber et al. (2015), radio-quiet QSOs remain on the MS, since they fall within a stellar mass regime where both the linear and curved MS agree. Therefore, the triggering of the activity in these galaxies is less likely to be related to rejuvenation.

8   CONCLUSION

Taking advantage of recent IR observing campaigns undertaken for the 2Jy sample, and the availability of archival IR data (see § 2), we investigated the triggering and feedback mechanisms of powerful radio AGNs, split in terms of SLRGs (i.e. showing strong optical emission lines, typically observed in QSOs) and WLRGs (i.e. lacking strong optical emission lines). To do this, we calculated dust masses (see § 3), tracing the cool ISM, and SFRs (see § 4), removing AGN contamination, for our samples of powerful radio AGNs, but also for our comparison samples of radio-quiet Type-I and Type-II QSOs, ULIRGs, and non-AGN classical elliptical galaxies.

---

[17] We stress that here we are comparing with the positions of the MS derived for objects pre-identified as star-forming galaxies, rather that those derived for samples that include a mixture of star-forming and quiescent, red and dead, elliptical galaxies (e.g. Eales et al. 2017), which tend to fall at lower SFRs for a given stellar mass and naturally show a curve at higher stellar masses.

We found that the cool ISM content of SLRGs is enhanced compared to that of non-AGN classical elliptical galaxies, yet below that of ULIRGs (see § 6.1). Galaxy mergers and interactions that are relatively minor in terms of their cool ISM contents are most likely responsible for this enhancement (see § 7.2). In contrast, the cool ISM contents of WLRGs associated with FRI-like radio jets are reduced when compared to SLRGs. This is also in contrast with the cool ISM properties of WLRGs/FRIIs, which were found more consistent with that of SLRGs. Therefore, while WLRG/FRIs are mostly triggered by different mechanisms (i.e. direct accretion of the hot gas), at least some WLRG/FRIIs may have been triggered in a similar way to the SLRGs but recently switched off (see § 7.2).

No relationships were found between the cool ISM content of our samples of AGNs and the power of the AGN, as traced by $L_{[OIII]}$ (see § 7.3). This implies that, while a minimum amount of gas of $M_{gas} \sim 10^8 M_\odot$ is required to trigger the mostly radiatively efficient radio AGNs, other factors must also be important in dictating the AGN power and efficiencies.

Finally, many of the powerful radio AGNs in our samples fall below the MS of Sargent et al. (2014), implying that their SFRs are lower than expected for galaxies at such stellar masses and redshifts (see §,7.5). We argued that this cannot be due to the quenching effect of AGN feedback on star formation, since it would be inconsistent the surprisingly high star formation efficiencies found in SLRGs, which are typical of those observed in star-bursting systems (see § 7.4). In fact, we further showed that the location of powerful radio AGNs in the R_{MS}-M_* parameter space coincides with that of a population of galaxies believed to be undergoing rejuvenation (see §,7.5).

Overall, our results provide strong evidence that the majority of powerful radio AGNs in the local universe are associated with late-time re-triggering of both star formation and AGN activity (rejuvenation), mainly fuelled via galaxy mergers and interactions for SLRGs, and some other mechanisms (e.g. direct accretion of the hot gas) for WLRGs.

and analysis: MATPLOTLIB (Hunter 2007), ASTROPY (Astropy Collaboration et al. 2018), NUMPY, SCIPY (Virtanen et al. 2020), PANDAS (McKinney 2010), MATH (Van Rossum 2020), and NUMBA (Lam et al. 2015).

DATA AVAILABILITY STATEMENT

The archival data of this article were accessed from the IRSA (`https://irsa.ipac.caltech.edu/frontpage/`) and the NED (`https://ned.ipac.caltech.edu`) databases. Other data (e.g. fluxes from targetted observations) are available in Tables referenced in the text. The new data generated by our analysis have been made available in the supplementary material of this publication.

REFERENCES

Adelberger K. L., Steidel C. C., 2005, ApJ, 630, 50

Akaike H., 1973, Biometrika, 60, 255

Akaike H., 1994, in Bozdogan H., Sclove S. L., Gupta A. K., Haughton D., Kitagawa G., Ozaki T., Tanabe K., eds, , Proceedings of the First US/Japan Conference on the Frontiers of Statistical Modeling: An Informational Approach: Volume 3 Engineering and Scientific Applications. Springer Netherlands, Dordrecht, pp 27–38, doi:10.1007/978-94-011-0854-6_2, `http://dx.doi.org/10.1007/978-94-011-0854-6_2`

Allen S. W., Dunn R. J. H., Fabian A. C., Taylor G. B., Reynolds C. S., 2006, MNRAS, 372, 21

Astropy Collaboration et al., 2018, AJ, 156, 123

Bell E. F., de Jong R. S., 2001, ApJ, 550, 212

Bell E. F., McIntosh D. H., Katz N., Weinberg M. D., 2003, ApJS, 149, 289

Bennett A. S., 1962a, Mem. RAS, 68, 163

Bennett A. S., 1962b, MNRAS, 125, 75

Bernhard E., Grimmett L. P., Mullaney J. R., Daddi E., Tadhunter C., Jin S., 2019, MNRAS, 483, L52

Bernhard E., Tadhunter C., Mullaney J. R., Grimmett L. P., Rosario D. J., Alexander D. M., 2021, MNRAS, 503, 2598

Best P. N., Kauffmann G., Heckman T. M., Brinchmann J., Charlot S., Ivezić Ž., White S. D. M., 2005, MNRAS, 362, 25

Best P. N., Kaiser C. R., Heckman T. M., Kauffmann G., 2006, MNRAS, 368, L67

Boroson T. A., Green R. F., 1992, ApJS, 80, 109

Boselli A., et al., 2010, PASP, 122, 261

Bundy K., Fukugita M., Ellis R. S., Targett T. A., Belli S., Kodama T., 2009, ApJ, 697, 1369

Buttiglione S., Capetti A., Celotti A., Axon D. J., Chiaberge M., Macchetto F. D., Sparks W. B., 2009, A&A, 495, 1033

Buttiglione S., Capetti A., Celotti A., Axon D. J., Chiaberge M., Macchetto F. D., Sparks W. B., 2010, A&A, 509, A6

Buttiglione S., Capetti A., Celotti A., Axon D. J., Chiaberge M., Macchetto F. D., Sparks W. B., 2011, A&A, 525, A28

Cappellari M., et al., 2011, MNRAS, 413, 813

Chabrier G., 2003, PASP, 115, 763

Chauke P., et al., 2019, ApJ, 877, 48

Ciesla L., et al., 2014, A&A, 565, A128

Clark C. J. R., Schofield S. P., Gomez H. L., Davies J. I., 2016, MNRAS, 459, 1646

Clemens M. S., Bressan A., Panuzzo P., Rampazzo R., Silva L., Buson L., Granato G. L., 2009, MNRAS, 392, 982

Clements D. L., et al., 2018, MNRAS, 475, 2097

Conroy C., White M., 2013, ApJ, 762, 70

Cortese L., et al., 2014, MNRAS, 440, 942

Costa T., Rosdahl J., Sijacki D., Haehnelt M. G., 2018, MNRAS, 473, 4197

Croom S. M., et al., 2005, MNRAS, 356, 415

Daddi E., et al., 2007, ApJ, 670, 156

Davis T. A., et al., 2015, MNRAS, 449, 3503

Davis T. A., Greene J. E., Ma C.-P., Blakeslee J. P., Dawson J. M., Pandya V., Veale M., Zabel N., 2019, MNRAS, 486, 1404

Di Matteo T., Springel V., Hernquist L., 2005, Nature, 433, 604

Dicken D., Tadhunter C., Axon D., Morganti R., Inskip K. J., Holt J., González Delgado R., Groves B., 2009, ApJ, 694, 268

Dicken D., et al., 2012, ApJ, 745, 172

Dicken D., et al., 2014, ApJ, 788, 98

Draine B. T., 2003, ARA&A, 41, 241

Draine B. T., Li A., 2007, ApJ, 657, 810

Dunlop J. S., McLure R. J., Kukula M. J., Baum S. A., O'Dea C. P., Hughes D. H., 2003, MNRAS, 340, 1095

Dunne L., Eales S. A., 2001, MNRAS, 327, 697

Eales S., de Vis P., Smith M. W. L., Appah K., Ciesla L., Duffield C., Schofield S., 2017, MNRAS, 465, 3125

Elbaz D., et al., 2007, A&A, 468, 33

Ellison S. L., Viswanathan A., Patton D. R., Bottrell C., McConnachie A. W., Gwyn S., Cuillandre J.-C., 2019, MNRAS, 487, 2491

Fabian A. C., 2012, ARA&A, 50, 455

Fanaroff B. L., Riley J. M., 1974, MNRAS, 167, 31P

Fazio G. G., et al., 2004, ApJS, 154, 39

Foreman-Mackey D., Hogg D. W., Lang D., Goodman J., 2013, PASP, 125, 306

Galliano F., Galametz M., Jones A. P., 2018, ARA&A, 56, 673

Gelderman R., Whittle M., 1994, ApJS, 91, 491

Genzel R., et al., 1998, ApJ, 498, 579

Giovannini G., Feretti L., Venturi T., Lara L., Marcaide J., Rioja M., Spangler S. R., Wehrle A. E., 1994, ApJ, 435, 116

Goldschmidt P., Miller L., La Franca F., Cristiani S., 1992, MNRAS, 256, 65P

Goodman J., Weare J., 2010, Communications in applied mathematics and computational science, 5, 65

Griffin M. J., et al., 2010, A&A, 518, L3+

Grimmett L. P., Mullaney J. R., Jin S., Bernhard E., Daddi E., Walters K., 2019, MNRAS, 487, 4071

Haas M., Siebenmorgen R., Schulz B., Krügel E., Chini R., 2005, A&A, 442, L39

Hardcastle M. J., Evans D. A., Croston J. H., 2007, MNRAS, 376, 1849

Harrison C. M., 2017, Nature Astronomy, 1, 0165

Heckman T. M., Smith E. P., Baum S. A., van Breugel W. J. M., Miley G. K., Illingworth G. D., Bothun G. D., Balick B., 1986, ApJ, 311, 526

Heckman T. M., Ptak A., Hornschemeier A., Kauffmann G., 2005, ApJ, 634, 161

Hinshaw G., et al., 2013, ApJS, 208, 19

Hunt L. K., et al., 2015, A&A, 576, A33

Hunter J. D., 2007, Computing in Science and Engineering, 9, 90

Inskip K. J., Tadhunter C. N., Morganti R., Holt J., Ramos Almeida C., Dicken D., 2010, MNRAS, 407, 1739

Jackson N., Rawlings S., 1997, MNRAS, 286, 241

James A., Dunne L., Eales S., Edmunds M. G., 2002, MNRAS, 335, 753

Jarrett T. H., Chester T., Cutri R., Schneider S., Skrutskie M., Huchra J. P., 2000, AJ, 119, 2498

Jarvis M. E., et al., 2020, MNRAS, 498, 1560

Juvela M., Ysard N., 2012, A&A, 541, A33

Kaviraj S., Peirani S., Khochfar S., Silk J., Kay S., 2009, MNRAS, 394, 1713

Kennicutt Jr. R. C., 1998, ApJ, 498, 541

Kokusho T., Kaneda H., Bureau M., Suzuki T., Murata K., Kondo A., Yamagishi M., 2017, A&A, 605, A74

Kokusho T., et al., 2019, A&A, 622, A87

Koss M., et al., 2017, ApJ, 850, 74

Lam S. K., Pitrou A., Seibert S., 2015, in Proceedings of the Second Workshop on the LLVM Compiler Infrastructure in HPC. LLVM '15. Association for Computing Machinery, New York, NY, USA, doi:10.1145/2833157.2833162, `https://doi.org/10.1145/2833157.2833162`

Lamperti I., et al., 2019, MNRAS, 489, 4389

Lanz L., Ogle P. M., Alatalo K., Appleton P. N., 2016, ApJ, 826, 29

Leahy J. P., Perley R. A., 1991, AJ, 102, 537

Leahy J. P., Pooley G. G., Riley J. M., 1986, MNRAS, 222, 753

Ludke E., Garrington S. T., Spencer R. E., Akujor C. E., Muxlow T. W. B., Sanghera H. S., Fanti C., 1998, MNRAS, 299, 467

Mack K. H., Klein U., O'Dea C. P., Willis A. G., 1997, A&AS, 123, 423

Maiolino R., Ruiz M., Rieke G. H., Papadopoulos P., 1997, ApJ, 485, 552

Malin D. F., Carter D., 1983, ApJ, 274, 534

Mancini C., et al., 2019, MNRAS, 489, 1265

Marconi A., Hunt L. K., 2003, ApJ, 589, L21

Martini P., 2004, in Ho L. C., ed., Coevolution of Black Holes and Galaxies. p. 169 (`arXiv:astro-ph/0304009`)

Marton G., et al., 2017, arXiv e-prints,

Mattsson L., Gomez H. L., Andersen A. C., Matsuura M., 2015, MNRAS, 449, 4079

McKinney W., 2010, in van der Walt S., Millman J., eds, Proceedings of the 9th Python in Science Conference. pp 51 – 56

McNamara B. R., Nulsen P. E. J., 2007, ARA&A, 45, 117

Morganti R., Killeen N. E. B., Tadhunter C. N., 1993, MNRAS, 263, 1023

Morganti R., Oosterloo T., Tadhunter C. N., Aiudi R., Jones P., Villar-Martin M., 1999, A&AS, 140, 355

Mountrichas G., Buat V., Georgantopoulos I., Yang G., Masoura V. A., Boquien M., Burgarella D., 2021, arXiv e-prints, p. arXiv:2106.11579

Mullaney J. R., Alexander D. M., Goulding A. D., Hickox R. C., 2011, MNRAS, 414, 1082

Nesvadba N. P. H., et al., 2010, A&A, 521, A65

Nesvadba N. P. H., et al., 2021, arXiv e-prints, p. arXiv:2103.12816

Noeske K. G., et al., 2007, ApJ, 660, L43

Orellana G., et al., 2017, A&A, 602, A68

Pandya V., et al., 2017, MNRAS, 472, 2054

Parkin T. J., et al., 2012, MNRAS, 422, 2291

Pearson C., et al., 2016, ApJS, 227, 9

Pierce J. C. S., et al., 2021, arXiv e-prints, p. arXiv:2111.03075

Pilbratt G. L., et al., 2010, A&A, 518, L1+

Poglitsch A., et al., 2010, A&A, 518, L2

Ramos Almeida C., Tadhunter C. N., Inskip K. J., Morganti R., Holt J., Dicken D., 2011, Monthly Notices of the Royal Astronomical Society, 410, 1550

Ramos Almeida C., et al., 2012, MNRAS, 419, 687

Rémy-Ruyer A., et al., 2014, A&A, 563, A31

Reyes R., et al., 2008, AJ, 136, 2373

Rieke G. H., et al., 2004, ApJS, 154, 25

Rieke G. H., Alonso-Herrero A., Weiner B. J., Pérez-González P. G., Blaylock M., Donley J. L., Marcillac D., 2009, ApJ, 692, 556

Rodighiero G., et al., 2014, MNRAS, 443, 19

Rodríguez-Zaurín J., Tadhunter C. N., Delgado R. M. G., 2010, Monthly Notices of the Royal Astronomical Society, 403, 1317

Rosario D. J., et al., 2018, MNRAS, 473, 5658

Saintonge A., et al., 2011, MNRAS, 415, 32

Saintonge A., et al., 2012, ApJ, 758, 73

Sanders D. B., Mirabel I. F., 1996, ARA&A, 34, 749

Sanders D. B., Soifer B. T., Elias J. H., Madore B. F., Matthews K., Neugebauer G., Scoville N. Z., 1988, ApJ, 325, 74

Sargent M. T., et al., 2014, ApJ, 793, 19

Saunders W., et al., 2000, MNRAS, 317, 55

Schaye J., et al., 2015, MNRAS, 446, 521

Schmidt M., Green R. F., 1983, ApJ, 269, 352

Schreiber C., et al., 2015, A&A, 575, A74

Schulz B., et al., 2017, arXiv e-prints,

Serra P., et al., 2012, MNRAS, 422, 1835

Shangguan J., Ho L. C., 2019, ApJ, 873, 90

Shangguan J., Ho L. C., Xie Y., 2018, ApJ, 854, 158

Shangguan J., Ho L. C., Bauer F. E., Wang R., Treister E., 2020, ApJ, 899, 112

Shen Y., et al., 2009, ApJ, 697, 1656

Shetty R., Kauffmann J., Schnee S., Goodman A. A., 2009, ApJ, 696, 676

Siebenmorgen R., Krügel E., 2007, A&A, 461, 445

Siebenmorgen R., Heymann F., Efstathiou A., 2015, A&A, 583, A120

Skrutskie M. F., et al., 2006, AJ, 131, 1163

Smethurst R. J., et al., 2016, MNRAS, 463, 2986

Smith E. P., Heckman T. M., 1989, ApJ, 341, 658

Smith M. W. L., et al., 2012, ApJ, 748, 123

Spinrad H., Djorgovski S., Marr J., Aguilar L., 1985, PASP, 97, 932

Stanley F., Harrison C. M., Alexander D. M., Swinbank A. M., Aird J. A., Del Moro A., Hickox R. C., Mullaney J. R., 2015, MNRAS, 453, 591

Stern J., Laor A., 2012, MNRAS, 426, 2703

Symeonidis M., 2017, MNRAS, 465, 1401

Tadhunter C., 2016, A&ARv, 24, 10

Tadhunter C. N., Morganti R., di Serego Alighieri S., Fosbury R. A. E., Danziger I. J., 1993, MNRAS, 263, 999

Tadhunter C. N., Morganti R., Robinson A., Dickson R., Villar-Martin M., Fosbury R. A. E., 1998, MNRAS, 298, 1035

Tadhunter C., et al., 2011, MNRAS, 412, 960

Tadhunter C. N., Ramos Almeida C., Morganti R., Holt J., Rose M., Dicken D., Inskip K., 2012, MNRAS, 427, 1603

Tadhunter C., Dicken D., Morganti R., Konyves V., Ysard N., Nesvadba N., Ramos Almeida C., 2014, MNRAS, 445, L51

Thomas D., Maraston C., Schawinski K., Sarzi M., Silk J., 2010, MNRAS, 404, 1775

Urry C. M., Padovani P., 1995, PASP, 107, 803

Van Rossum G., 2020, The Python Library Reference, release 3.8.2. Python Software Foundation

Virtanen P., et al., 2020, Nature Methods,

Vlahakis C., Dunne L., Eales S., 2005, MNRAS, 364, 1253

Wall J. V., Peacock J. A., 1985, MNRAS, 216, 173

Werner M. W., et al., 2004, ApJS, 154, 1

Westhues C., et al., 2016, AJ, 151, 120

White M., et al., 2012, MNRAS, 424, 933

Wright E. L., et al., 2010, AJ, 140, 1868

Yesuf H. M., Ho L. C., 2020, ApJ, 901, 42

Young L. M., et al., 2011, MNRAS, 414, 940

Zhang Z., Shi Y., Rieke G. H., Xia X., Wang Y., Sun B., Wan L., 2016, ApJ, 819, L27

Zubovas K., King A., 2012, ApJ, 745, L34

This paper has been typeset from a TEX/LATEX file prepared by the author.